DISSERTATION

UNDERSTANDING SELECTIVITY IN ORGANIC REACTIONS THROUGH DENSITY FUNCTIONAL THEORY

Submitted by

Louis Raymond Philibert de Lescure

Department of Chemistry

In partial fulfillment of the requirements

For the Degree of Doctor of Philosophy

Colorado State University

Fort Collins, Colorado

Summer 2024

Doctoral Committee:

Advisor: Robert Paton,
Co-Advisor: Andrew McNally

Jeffrey Bandar
Alan Kennan
Margarita Herrera-Alonso

ABSTRACT

UNDERSTANDING SELECTIVITY IN ORGANIC REACTIONS THROUGH DENSITY FUNCTIONAL THEORY

The success of chemical reactions is often expressed through the lens of selectivity, defined as the preference for a desired reaction pathway over an undesirable one. A profound understanding of the rationale behind the selectivity of chemical reactions is crucial for the progression of synthetic methodologies in organic chemistry. Utilizing quantum chemical approximations, density functional theory (DFT) calculations offer unparalleled insights into the electronic structures and mechanisms of reactions, which can be correlated with observed empirical selectivities.

This dissertation demonstrates the significant utility of DFT, in tandem with experimental evidence, in elucidating the intricate mechanisms of reactions. Chapter 1 defines the thematic and methods used throughout this thesis.

Chapters 2 and 3 detail collaborative work with the McNally group at Colorado State University. Here, we developed innovative methods for the halogenation of pyridines and advanced modifications of pyrimidine rings utilizing redesigned Zincke chemistry. This chapter focuses on the factors influencing the regioselectivity of halogenation processes and provides mechanistic insights into the formation of crucial intermediates.

Chapter 3 outlines a joint project with the Race group at the University of Minnesota, where we explored the homologation of benzylic carbon-bromide bonds. Our investigations centered on the ring-opening of phenonium intermediates, a critical step in determining the success of the reaction.

Chapter 4 presents a collaboration with the Aggarwal group at the University of Bristol. This chapter examines the nuanced interplay between kinetic and thermodynamic factors that govern the enantioselectivity of the reaction discussed. This comprehensive study underscores the integration of theoretical and experimental approaches in advancing our understanding of complex chemical reactions.

ACKNOWLEDGMENTS

First and foremost, I would like to express my profound gratitude to my advisors, Dr. Robert Paton, and Dr. Andrew McNally, for their unwavering support and guidance throughout my time at Colorado State University. Their insights and expertise have been invaluable, and I am very grateful for the opportunities they have offered me throughout my PhD.

I am also deeply thankful to the Paton, McNally and Kim Lab members for their collaboration, scientific insights, and camaraderie. Special thanks to Dr. Juan Vicente Alegre Requena for being a fantastic mentor and friend and Dr. Guilian Luchini and Dr. Heidi Klem for being awesome roommates and friends throughout this journey.

I also want to thank my (soon to be) wife Krystal Hopkins whose support and love have been my anchor throughout this journey. Lastly, I would like to thank my family: my parents, Benoît and Agnès, and my siblings Jeanne and Alice for their unconditional love and support. They have always believed in me, even when I doubted myself, and their constant encouragement and belief in my abilities have been my pillar of strength. This thesis would not have been possible without the contributions of each of these individuals, and for that, I am eternally grateful.

Cette Thèse est dédiée à la mémoire de mon père, qui a travers ces valeurs et son amour continue de me guider chaque jour. Il m’a transmis sa passion pour la science et ma continuellement encourager à poursuivre mes études dans la recherche. J’espère honorer son héritage à travers ma

passion continue pour l’apprentissage et le partage du savoir. Je t’aime papa, on se reverra dans les étoiles.

TABLE OF CONTENTS

CHAPTER 1: INTRODUCTIONS.

1.1 Selectivity in chemical reactions

Understanding the outcomes of chemical reactions is fundamental in the development of innovative reactions based on established methodologies. In chemistry, the success and efficiency of a reaction are often evaluated in terms of selectivity, which has three principal types: chemoselectivity, regioselectivity, and enantioselectivity. These terms define the preference between two or more competing chemical pathways in a reaction.

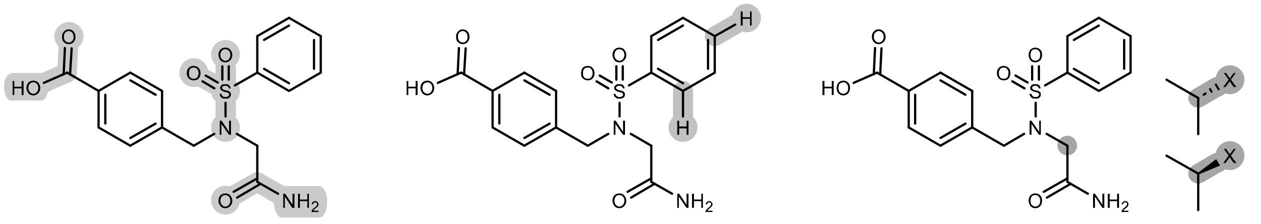

Chemoselectivity Regioselectivity Enantioselectivity

Figure 1.1 Different forms of selectivity.

Chemoselectivity involves the selective reaction of a specific reactant with one of several possible functional groups in a complex molecule. This selective behavior is vital for synthesizing complex organic molecules, as it ensures that only designated sites within the molecule are altered, leaving other reactive groups unaffected.

Regioselectivity concerns the preference for forming a chemical bond at a particular site over other viable locations within a molecule when multiple chemically similar possibilities exist. This selectivity is essential for the structural modification of complex molecules, which might possess many iterations of the same functionality, ensuring that changes occur precisely where intended.

Enantioselectivity refers to the preference of a chemical reaction to produce one enantiomer over another. Enantiomers are molecules with identical connectivity that are mirror images of one another. Because enantiomers can exhibit significantly different biological activities, high enantioselectivity is particularly critical in the pharmaceutical, agricultural, and food industries.

In industries such as pharmaceuticals and materials, selectivity is crucial for the precise manipulation of multiple functional groups within complex molecules. Efficient drug synthesis, for example, relies heavily on the selective transformation of specific moieties without altering the rest of the molecule.

To understand and predict the behavior of chemical reactions, it is necessary to rationalize selectivity. There is a significant push in both industry and academia toward developing robust models that can predict selectivity based on an understanding of underlying chemical mechanisms. While experimental studies of reaction rates provide direct data, they can be complex and offer limited insight into the factors controlling selectivity. Alternatively, ab initio and semi-empirical methods allow for the examination of the electronic structures of intermediate species along a reaction pathway and their relative energies. By applying these methods, we can gain insights into the kinetic and thermodynamic behaviors of reactions, and understand the factors driving selectivity, including crucial intermolecular and intramolecular interactions. This thesis focuses on the application of computational methods to the elucidation of reaction mechanisms and rationalization of selectivity.

1.2 Computational methods

1.2.1 Density Functional Theory

The theoretical foundation of DFT is rooted in the Hohenberg-Kohn theorems, first published in 1964.[1] These theorems revolutionized the approach to solving the Schrödinger equation for electrons in a system. The First Theorem states that the ground state properties of a many-electron system is a unique functional of the electron density, rather than the many-body wavefunction. This implies that the electron density, a function of three spatial coordinates, contains all necessary information about the system, simplifying the complex many-body problem significantly. The Second Theorem establishes the variational principle for the electron density, enabling the development of practical methods to calculate the density in a manner that minimizes the total energy. These theorems shifted the focus from the wavefunction to the electron density as the fundamental quantity of interest, which simplified the computational requirements for many-electron systems.

One of the most active areas of DFT research involves the development of exchange-correlation (XC) functionals.[2] The accuracy of DFT calculations depends critically on these functionals, which approximate the many-body interaction terms in the Kohn-Sham equations. Initially, the local density approximation (LDA) was used, where the XC energy is a function solely of the electron density at a point. While LDA has been remarkably successful in predicting the properties of many systems, its accuracy is limited for systems with strong electronic localization or delocalization. To improve upon LDA, gradient-corrected functionals (GGA) were developed. These consider not only the density but also its first derivatives. Later, hybrid functionals, which mix Hartree-Fock exact exchange with DFT exchange, provided further improvements in treating systems where LDA and GGA fall short.

Modern developments in DFT also focus on computational aspects. The advent of high-performance computing has enabled the application of DFT to increasingly large and complex systems. Algorithms like the projector augmented wave method and the introduction of linear scaling DFT methods have significantly reduced the computational cost.[3] Alternative semi-empirical methods are also emerging as an efficient alternative to DFT.

1.2.2 Semi-empirical methods

Semi-empirical methods in quantum chemistry are computational techniques that balance computational efficiency and reasonable accuracy for large molecular systems by incorporating empirical parameters into their models. These methods simplify the electronic Hamiltonian and reduce computational overhead by using parameterized formulas that are derived from experimental data or higher-level calculations. A prominent example of a modern semi-empirical method is the extended tight-binding (XTB) model, which significantly extends the applicability of semi-empirical approaches.[4] XTB uses a minimal basis set and approximates the electronic Hamiltonian to achieve faster computations, making it particularly useful for large-scale dynamics simulations and for systems where traditional DFT calculations would be too slow. Despite its empirical nature, XTB has been designed to offer a good balance between speed and accuracy, providing useful insights in systems ranging from small organic molecules to large biomolecular complexes.

1.2.3 Connecting computations with experiments

DFT serves as a bridge between theoretical chemistry and practical experimental applications. By providing a deep understanding of the fundamental molecular behavior through free energy surfaces, transition state theory, Quantitative Structure Activity Relationship (QSAR) studies, and electronic structures, DFT enhances the design, execution, and interpretation of experiments. This synergy not only advances our theoretical knowledge but also drives innovation in material science, pharmaceuticals, and beyond, illustrating the profound impact of computational chemistry in contemporary research.

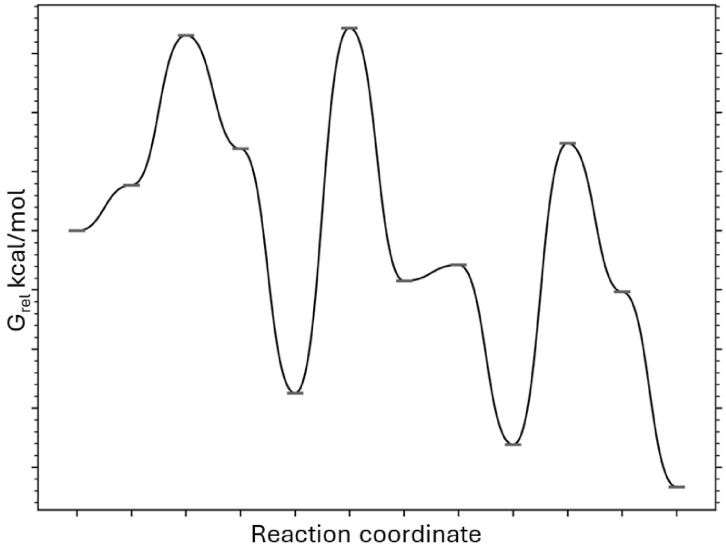

Figure 1.2 An example free energy surface

Free energy surfaces (FES) provide a topographical representation of the energy changes associated with different molecular configurations and states during a reaction **(Figure 1.2)**. DFT can be used to calculate these surfaces by evaluating the changes of free energy of a system at various points along a reaction coordinate. We can use these changes in free energy to identify key transition states and their activation energy. The Eyring-Polanyi equation, integral to transition state theory, offers a detailed and quantifiable approach to understanding the kinetics of chemical reactions. This theory conceptualizes a 'transition state', a high-energy, intermediate stage through which reactants must pass before transforming into products. The equation specifically quantifies the rate at which these transitions occur, linking the reaction rate to activation energies and temperature.

Mathematically, the Eyring equation is expressed as:

$$k = \frac{k_B T}{h} e^{-\frac{\Delta G^{\ddagger}}{RT}}$$

Here, k represents the reaction rate constant, indicating how quickly a reaction proceeds. k_B and h are fundamental constants, Boltzmann's constant and Planck's constant, respectively. T denotes the absolute temperature, providing insight into how temperature influences reaction speeds. The term $\Delta G^{\ddagger}$ is the Gibbs free energy of activation. It represents the energy barrier that must be overcome for reactants to transform into products. This barrier is crucial because it determines the sensitivity of the reaction rate to temperature changes, a key principle in chemical kinetics. R is the universal gas constant, linking the energy dimensions in the equation.

The pre-exponential factor $\frac{k_B T}{h}$ indicates the frequency with which reactants approach the transition state. It combines thermodynamic and quantum mechanical elements, suggesting that reaction rates are influenced by both the thermal energy of the reactants and the quantum mechanical probability of transitioning past the energy barrier. Kinetic experiments are often designed to measure reaction rates and activation energies, which can then be compared directly to the predictions made by DFT calculations through TST. This comparison is vital for validating the accuracy of DFT methods and for refining the models based on experimental data.

Quantitative Structure-Activity Relationships (QSAR) are used extensively in the design of drugs and new materials, predicting the properties and activities of compounds based on their structural attributes. DFT provides a robust framework for calculating these properties, which are used as descriptors in QSAR models. The properties calculated via DFT, such as dipole moments, electronic affinities, and ionization potentials, are used to develop QSAR models. These models can be used by practitioners to predict molecular properties and guide reaction design, thereby speeding up the development process and improving the efficiency of discovering new materials and pharmaceuticals.

DFT also offers insight into the electronic structure of molecules. Properties such as electron density, molecular orbitals and their associated energy levels are crucial for understanding a wide range of chemical properties and behaviors. This theoretical data is essential for interpreting results from spectroscopic experiments like NMR, IR, UV-Vis, and X-ray crystallography. By comparing the electronic structures predicted by DFT with experimental spectra, chemists can elucidate molecular structures, identify functional groups, and understand the dynamics of electron movements within molecules.

1.3 Introduction to tools and software

This section introduces various tools and software used throughout this thesis.

1.3.1 Goodvibes

Goodvibes is a software developed by the Paton lab that is designed to facilitate the thermodynamic analysis of computed chemical structures and reactions using quantum chemistry output files.[5] It primarily focuses on correcting and refining Gibbs free energy calculations, particularly in the context of exploring reaction mechanisms and kinetics. The tool applies vibrational frequency analysis to estimate the thermodynamic properties of molecules at different temperatures and pressures. By using quasi-harmonic oscillator models and other thermodynamic corrections, Goodvibes can provide more accurate calculation of free energy changes in chemical reactions, which are crucial for understanding reaction feasibility and conditions.

1.3.2 Conformational analysis

CREST (Conformer Rotamer Ensemble Sampling Tool) is the main tool used throughout this thesis to explore the conformational space of the molecules associated with the projects; it is a powerful tool used for generating low-energy conformers of molecules based on the GFN-xTB semi-empirical method.[6] It is particularly useful in handling large flexible molecules where exhaustive quantum mechanical calculations would be prohibitively expensive.

Alternatively, RDKit is an open-source cheminformatics toolkit that provides a wide array of software tools for handling chemical informatics tasks such as molecular visualization, generation of molecular descriptors, chemical reaction analysis, and more.[7] It is commonly used for conformational analysis where computational efficiency and integration with other data processing workflows are required.

1.3.3 Electronic structure analysis

To visualize and understand electronic structures, practitioners utilize Natural Bond Orbital (NBO) analysis.[8] This technique aids in comprehending the distribution of electron density within molecules by simplifying complex wavefunctions into a more chemically intuitive description that includes bonding and non-bonding orbitals. Such simplifications are instrumental in rationalizing chemical properties and reactivities. Additionally, electrostatic potential maps are employed to visualize the distribution of electric potential across a molecule. These maps provide valuable insights into how molecules might interact with other charged entities, predicting sites of reactivity, understanding hydrogen bonding interactions, and aiding in the design of molecules with specific electrostatic properties.

1.3.4 Breaking down molecular interactions

The ability to break down molecular interactions is crucial to identify which interactions are key in controlling selectivity or reactivity. Distortion Interaction Analysis is a method that decomposes the energy changes during chemical reactions into distortion and interaction components.[9] This separation helps in understanding the contribution of structural changes and electronic interactions to the overall reaction energy. Absolutely Localized Molecular Orbitals Energy Decomposition Analysis (ALMO EDA) is another sophisticated tool for dissecting intermolecular interactions into meaningful chemical concepts such as electrostatics, polarization, and charge transfer, among others.[10]

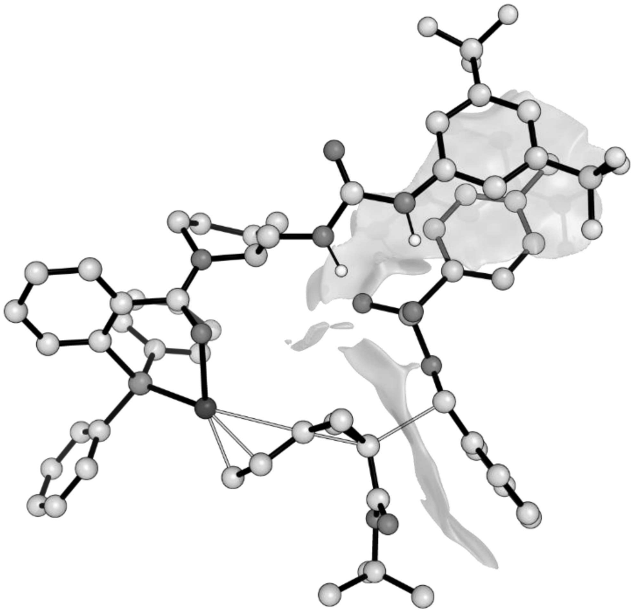

Figure 1.3 NCIplot showing non-covalent interactions between a ligand-metal complex and a substrate.

For a more qualitative approach NCIplot (Non-Covalent Interaction Plot) is a visualization tool that uses reduced density gradient techniques to identify and visualize non-covalent interactions within and between molecules **(Figure 1.3)**.[11] It is invaluable for exploring weak interactions that are critical in molecular recognition, enzyme function, and the stability of supramolecular complexes.

REFERENCES

1. P. Hohenberg; W. Kohn, *Phys. Rev.* 136, B864-B871 (1964); W. Kohn; L. J. Sham, *Phys. Rev.* 140, A1133-A1138 (1965)

2. C. J. Cramer, Essentials of Computational Chemistry, Theories and Models. 2nd ed.; John Wiley & Sons: Chichester, 2004; L. Goerigk, A. Hansen, C. Bauer; S. Ehrlich, A.Najibi, S. Grimme, *Phys. Chem. Chem. Phys.* 19, 32184-32215 (2017)

3. R. O. Jones, *Rev. Mod. Phys.* 87, 897 (2015)

4. C. Bannwarth, S. Ehlert, S. Grimme *J. Chem. Theory Comput*. 15, 3, 1652–1671 (2019)

5. G. Luchini, J. V. Alegre-Requena, I. Funes-Ardoiz, R. S. Paton *F1000 Research* (2020)

6. P. Pracht, F. Bohle, S. Grimme, *Phys. Chem. Chem. Phys.* 22, 7169-7192 (2020)

7. RDKit: Open-source cheminformatics. https://www.rdkit.org

8. E. D. Glendening, J. K. Badenhoop, A. E. Reed, J. E. Carpenter, J. A. Bohmann, C. M. Morales, P. Karafiloglou, C. R. Landis, and F. Weinhold, Theoretical Chemistry Institute, University of Wisconsin, Madison (2018).

9. F. M. Bickelhaupt, K. N. Houk, *Angew. Chem. Int. Ed.* 56, 34, 10070-10086 (2017)

10. P. R. Horn, Y. Mao, M. Head-Gordon, *Phys. Chem. Chem. Phys.* 18, 23067-23079 (2016)

11. J. Contreras-Garcia, E. R. Johnson, S. Keinan, R. Chaudret, J.-P. Piquemal, D. N. Beratan, W. Yang. *J. Chem. Theory Comput.* 7, 3, 625-632 (2011)

CHAPTER 2: C3 SELECTIVE HALOGENATION OF PYRIDINES THROUGH ZINCKE IMINES.

This chapter presents the computational work that elucidates the source of regioselectivity in a halogenation reaction of Zincke imine intermediates used as a novel way to achieve pyridine halogenation.

This work is the result of a collaboration with Benjamin Boyle and Jeffrey Levy from Andrew McNally's research group. All experimental work was performed by B.B. and J.L. all calculations were performed by L.d.L. This work was published as "Halogenation of the 3-position of pyridines through Zincke imine intermediates" in *Science* (378, 6621, 773-779, 2022).

2.1 Background and significance

2.1.1 Pyridine Halogenation

Pyridines are commonly found in molecules of biological importance; their widespread presence is attributed to the combined effects of the heterocycle's inherent electronic characteristics and various substituents.[1-4] Hence, regioselective halogenation of pyridine C–H bonds is crucial, as the formation of a carbon–halogen (C–Hal) bond facilitates a multitude of reactions. In the fields of pharmaceutical and agrochemical research, halogenated pyridines serve as critical intermediates for diversifying compound candidates for structure-activity relationship studies and targeted synthesis.[5-10] Such halogenated compounds, including etoricoxib, hold intrinsic value in bioactive substances. Nonetheless, despite the documentation of pyridine halogenation techniques since the late 19th century, significant challenges in this essential bond formation persist.[11-13] Specifically, methods selective for the 3-position often show incompatibility with many complex, biologically relevant substrates due to their sensitive functional groups.[14] Pyridine halogenation via electrophilic aromatic substitution presents an electronically mismatched process necessitating severe conditions.[15,16] Typically, the use of elemental halides with potent Brønsted or Lewis acids catalysts at high temperatures is needed to offset the low π nucleophilicity of pyridine rings.[5,6] The scope of substrates is restricted, and even though the reactions aim for 3-selectivity, they frequently yield regioisomeric mixtures. The metalation-halogenation strategy with strong bases represents another method for halogenating pyridines, yet most approaches require directing groups for consistent access to the 3-position.[17-19] Beyond these methodologies, advancement has been scarce over the last century, prompting the synthetic community to explore more versatile functional groups instead of halides. The most prominent of these are iridium-catalyzed borylations and silylations, achieving 3-selectivity for certain substituted pyridines or through ligand design.[20-26]

We introduce a novel strategy for pyridine halogenation that employs a ring-opening, halogenation, and ring-closing technique. This single-step method leverages an adapted version of the traditional Zincke ring-opening reaction, transforming pyridines into azatriene intermediates, or "Zincke imines" **(Figure 2.1)**. This approach momentarily changes pyridines from electron-poor heterocycles into polarized alkenes, which then undergo electrophilic substitution reactions akin to electron-rich aromatic compounds.

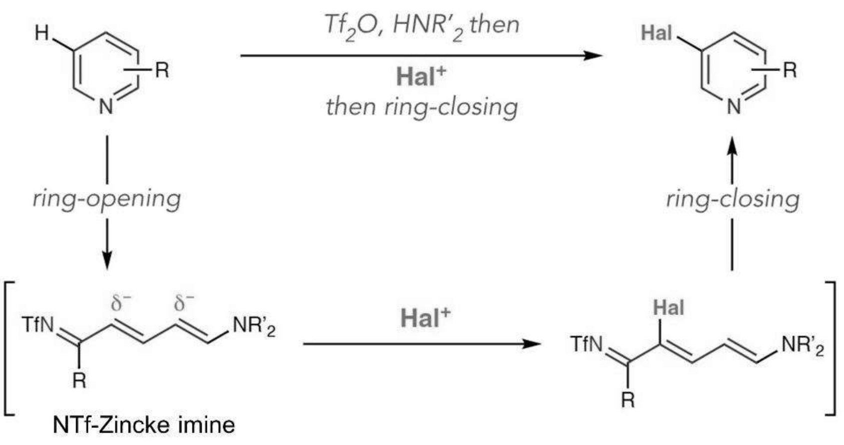

Figure 2.1 Strategy for pyridine halogenation through Zincke imines.

2.1.2 Zincke Reaction

The Zincke Reaction typically starts with the *N*-arylation of pyridine with a deficient chloro benzene such as 2,4-dinitrochlorobenzene to form a pyridinium salt. This is followed by the nucleophilic attack on the pyridinium ring with a secondary amine, which opens the ring and forms a Zincke intermediate (typically Zincke aldehyde). Subsequent reactions can then be tailored to introduce various substituents or functional groups, ultimately leading to a wide array of compounds from a relatively simple pyridine starting material.

Existing techniques for Zincke ring-opening chemistry are not sufficient to facilitate the generalized method for halogenating pyridines. The activation of the pyridine nitrogen demands harsh conditions and frequently does not proceed when substituents are located at the 2-position. This constraint disqualifies numerous categories of substituted pyridines.

2.2 Experimental findings

In our efforts to overcome the limitations inherent to the Zincke reaction, we directed our attention to the ring-opening reactions involving NTf-pyridinium salts. These intermediates are efficiently generated from pyridine and Tf_2O at low temperatures and are compatible with a broad array of substitution patterns, except for 2,6-disubstituted variants. Although Toscano et al. have demonstrated ring opening with Tf_2O, their investigations were confined to pyridine and resulted in a mixture of ring-opened entities.[30] Using 2-phenylpyridine, we explored various aliphatic amines as potential nucleophiles **(Figure 2.2)**. Compounds such as pyrrolidine, piperidine, and morpholine, alongside diisobutylamine, yielded moderately successful ring-opened products. Notably, dibenzylamine emerged as the most effective, yielding the Zincke imine product with high efficiency. We also expected that the ring-closing step for Zincke imines like would be straightforward, drawing from existing practices in analogous Zincke systems[31] Such as strategies involving ammonium salts or Brønsted acids to synthesize pyridines. These strategies were successful in ring closing the Zincke imine back to the pyridine.

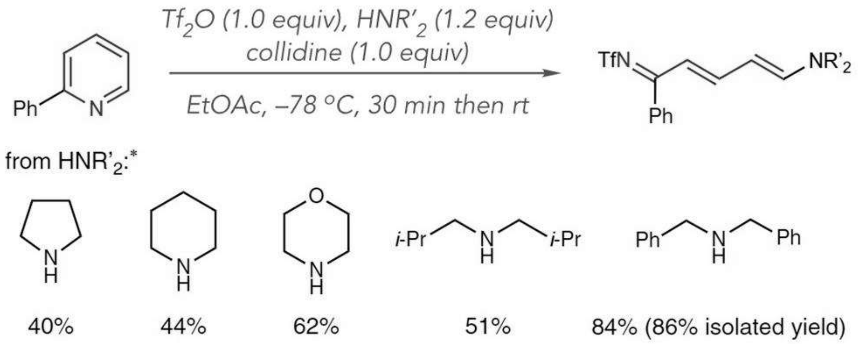

Figure 2.2 Ring opening of pyridines using Tf_2O and secondary amines.

In the subsequent phase of our research, we evaluated the reactivity of a 2Ph Zincke imine with various halogenating agents **(Figure 2.3)**. Initially, we had reservations about achieving selectivity in C–Hal bond formation, given the lack of an apparent electronic preference between the δ^- sites at C3 and C5 in the Zincke imine.[32] While Toscano et al. noted a 3-selective halogenation for an NTf-Zincke imine without substitutions derived from pyridine, they did not explore Zincke imines from substituted pyridines.[30] Treating 2Ph-Zincke imine with N-iodosuccinimide (NIS) at room temperature for 5 minutes yielded the iodinated product with a 92% yield and a selectivity ratio exceeding 20:1 for the 3- vs. 5-position, as determined by crude ^{1}H NMR analysis. Similarly, application of N-bromosuccinimide (NBS) yielded a mixture with a 4.4:1 ratio of C3 to C5 at room temperature, and a greater than 20:1 selectivity along with 92% yield of C3 iodinated product at -78°C in CH_2Cl_2. Chlorination using N-chlorosuccinimide (NCS) was less effective, both in yield and selectivity, leading to decomposition of the Zincke imine. Subsequent experiments on ring closure revealed that heating C3 iodinated Zincke imines in a solvent mix of EtOAc/EtOH at 60°C with ammonium acetate smoothly produced 3-iodopyridine.

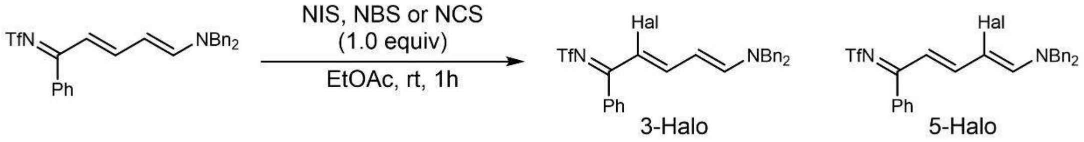

NXS / conditions	3-Halo (%)	5-Halo (%)
NIS (5 mins)	92	0
NBS	75	17
NBS, –78 ºC, CH_2Cl_2	92	1
NCS	6	21

Figure 2.3 Halogenation of 2-substituted Zincke imines.

For halogenating 3-substituted Zincke imines **(Figure 2.4)**, a modified approach was required. Opening of the 3-phenylpyridine ring resulted in the Zincke imine with an 82% yield, but it remained unreactive to NIS at room temperature and degraded upon heating to 50°C. Adding two equivalents of trifluoroacetic acid (TFA) led to the formation of the iodopyridine with high efficiency.[33] This enhanced reactivity is attributed to steric hindrance between the 3- and 5-substituents in the Zincke imine structure, with TFA facilitating the alkene isomerization-recyclization sequence, along with the removal of dibenzylamine and cleavage of the N–S bond in the NTf-pyridinium salt, reinstating the pyridine ring. Employing NBS and TFA for bromination achieved similar results, and a revised protocol using NCS with HCl in CH_2Cl_2 effectively chlorinated the Zincke imine. These findings offer two distinct halogenation methods for NTf-Zincke imine intermediates, adaptable based on their substitution patterns.

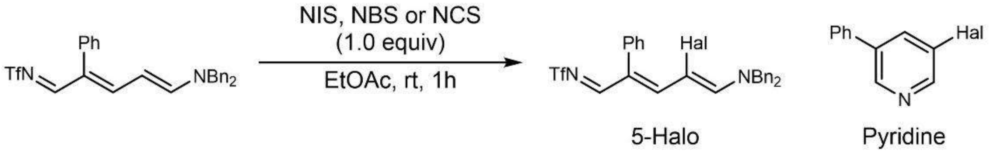

NXS / conditions	5-Halo	Pyridine (%)
NIS	0	0
NIS + TFA (2.0 eq)	0	90
NBS + TFA (2.0 eq)	0	76
NCS (1.2 eq) + HCl (4.0 eq), CH_2Cl_2	0	76

Figure 2.4 Halogenation of 3-substituted Zincke imines.

2.3 Computational findings

2.3.1 Methods

We further investigated the mechanism and regioselectivity of halogenation of Zincke imines using N-halosuccinimides through quantum chemical studies at the B3LYP-D3(BJ)/def2-TZVP//ωB97X-D/6-31+G(d,p) level, incorporating a "solvation model based on density (SMD)" for CH_2Cl_2. The calculated $\Delta\Delta G^{\ddagger}$ values remained broadly consistent across different computational methods **(Figure 2.5)**, indicating that the predictions for regioselectivity of any particular elementary step are fairly stable (variations < 1 kcal/mol). Yet, the absolute heights of the energy barriers exhibited more significant differences, with the ωB97X-D or M062X theories predicting Gibbs energy barriers that are notably higher compared to those observed at experimental reaction temperatures. Overall, the single point calculations using B3LYP-D3(BJ)/def2-TZVP accurately align with experimental results for all examined halogenations, offering both precise $\Delta\Delta G^{\ddagger}$ values and reasonable estimates of $\Delta G^{\ddagger}$ values.

LoT	TS-I-C3-NCS	TS-I-C5-NCS	$\Delta\Delta G^{\ddagger}$
B3LYP-D3(BJ)/def2-TZVP	22.4	22.9	0.5
M062X/def2-TZVP	29.6	29.6	0.0
ωB97X-D/def2-TZVP	28.9	28.6	0.3

LoT	TS-I-C3-NBS	TS-I-C5-NBS	$\Delta\Delta G^{\ddagger}$
B3LYP-D3(BJ)/def2-TZVP	19.3	21.9	2.6
M062X/def2-TZVP	25.0	26.8	1.8
ωB97X-D/def2-TZVP	23.7	25.1	1.4

LoT	TS-II-C3-NIS	TS-II-C5-NIS	$\Delta\Delta G^{\ddagger}$
B3LYP-D3(BJ)/def2-TZVP	22.2	25.6	3.4
M062X/def2-TZVP	24.7	27.5	2.8
ωB97X-D/def2-TZVP	21.9	24.9	3.0

Figure 2.5 Gibbs free energies with different single point energy corrections for ωB97X-D/6-31+G(d,p) stationary points.

2.3.2 Free energy surface for the ring opening of 2Ph pyridine

First, we investigated the mechanism of ring opening of 2Ph pyridine using dibenzyl amine **(Figure 2.6)**. The reaction begins with addition of dibenzyl amine to the NTf-pyridinium at the C2 with a low barrier of 5.6 kcal mol^{-1} which yields Int-I-C2 in an exergonic fashion (-7.7 kcal mol^{-1}). Exergonic deprotonation using collidine yields Int-DHP-C2 at -23.3 kcal mol^{-1}. This intermediate undergoes rapid ring opening via TS-RO and a barrier of 10 kcal mol^{-1} to give the Zincke imine product. The formally 6π pericyclic ring opening has a low barrier relative to its analogous hexatriene cyclization which has a barrier of 16 kcal mol^{-1}. We questioned which factors influence this transition state, and using NICS(0)$_{zz}$ values we looked at the aromaticity of the transition states. The cyclization of hexatriene has a NICS(0)$_{zz}$ value of -29.5 ppm indicating the expected highly aromatic structure. In contrast the ring closing of Int-DHP-C2 has NICS(0)$_{zz}$ of +4.9 ppm indicating there is little to no aromatic character in this TS. This ring opening occurs primarily through a polar mechanism involving both nitrogen lone pairs and their respective π* orbitals.

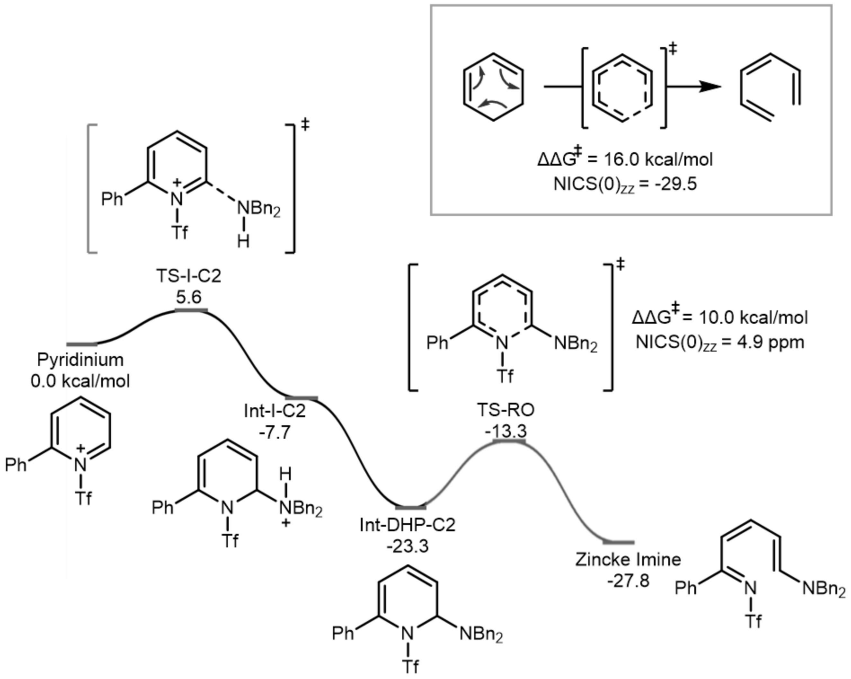

Figure 2.6 Free energy surface for the ring opening of NTf-pyridinium with dibenzyl amine and collidine. The polar character of TS-RO is exemplified through NICS(0)$_{zz}$ values calculated at the B3LYP/6-311+G(d,p) level of theory.

2.3.3 Electronic structures of Zincke Adduct

We performed calculations of NBO partial charge, Fukui indices, natural population, natural charge, and HOMO coefficients (using wb97xd/6-31+g(d,p)) for the most stable conformation of the 2Ph Zincke imine **(Figure 2.7)**. The f^- Fukui index, which helps gauge reactivity, is derived from the change in natural population (from NBO calculations) at a specific atom when comparing the neutral molecule to its oxidized form. Similarly, the f^+ Fukui index is calculated based on the difference in natural population at an atom when comparing the neutral molecule to its reduced state.

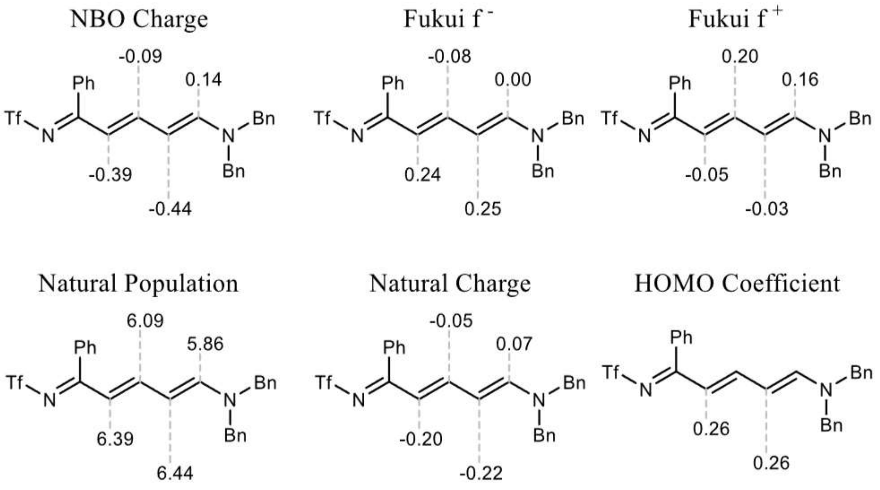

Figure 2.7 Natural populations, Fukui *f*$^-$, Fukui *f*$^+$ indices and HOMO coefficients for 2Ph substituted Zincke Imine.

Regioselectivity in electrophilic halogenation is traditionally interpreted through differences in frontier orbital coefficients, atomic charges, or nucleophilicity parameters.[34] Yet, for the C3 and C5 positions of Zincke imine 6, the electronic characteristics appear remarkably similar, with Fukui *f*$^-$ indices (0.24 vs. 0.25), natural charges (–0.39 vs. –0.44), and HOMO coefficients (both 0.26) indicating comparable reactivities, prompting the need for an alternative explanation for the pronounced C3 selectivity observed in this reaction.

2.3.4 Single electron initiation

We also investigated the potential for the reaction to initiate through a single electron transfer (SET) mechanism from the imine to the N-halosuccinimide **(Figure 2.8)**. This initiation route was determined to be energetically too costly to serve as a viable pathway. The Gibbs free energy (ΔG) of the SET process from the 2Ph substituted Imine to NIS, NBS, and NCS were found to be 34.1, 38.7, and 35.6 kcal/mol, respectively. These calculations were performed using the ωB97X-D/6-31+G(d,p) level of theory without a single point.

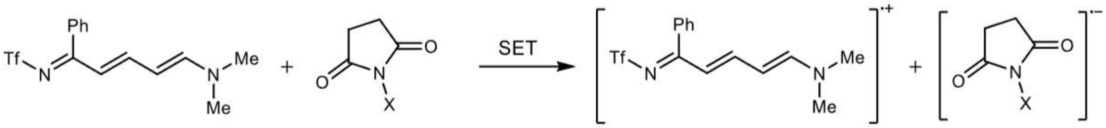

Figure 2.8 Single Electron transfer initiation from Zincke Imine to *N*-Halosuccinimide to generate a radical anion intermediate.

2.3.4 Two electron potential energy surfaces

Calculated energy profiles **(Figure 2.9)** for the reaction of a 2Ph Zincke imine with NCS, NBS, and NIS indicate that the overall reaction is irreversible, governed by kinetically controlled regioselectivity for each halogenation, with $\Delta\Delta G^{\ddagger}$ values closely matching experimental observations. The process of disrupting the extended conjugation in Zincke imine to form the high-energy σ-complex intermediate Int-I is energetically uphill: the relative Gibbs free energy (G_{rel}) of this intermediate escalates with the formation of C–Cl, C–Br, and C–I bonds, in ascending order (9.0, 13.7, and 19.7 kcal/mol, respectively). These energetic distinctions lead to two separate regimes dictating selectivity: the irreversible formation of the C–Hal bond (transition state TS-I) establishes regioselectivity for chlorination and bromination, whereas the formation of the C–I bond is reversible, making the second deprotonation step (transition state TS-II) crucial in determining regioselectivity.[35]

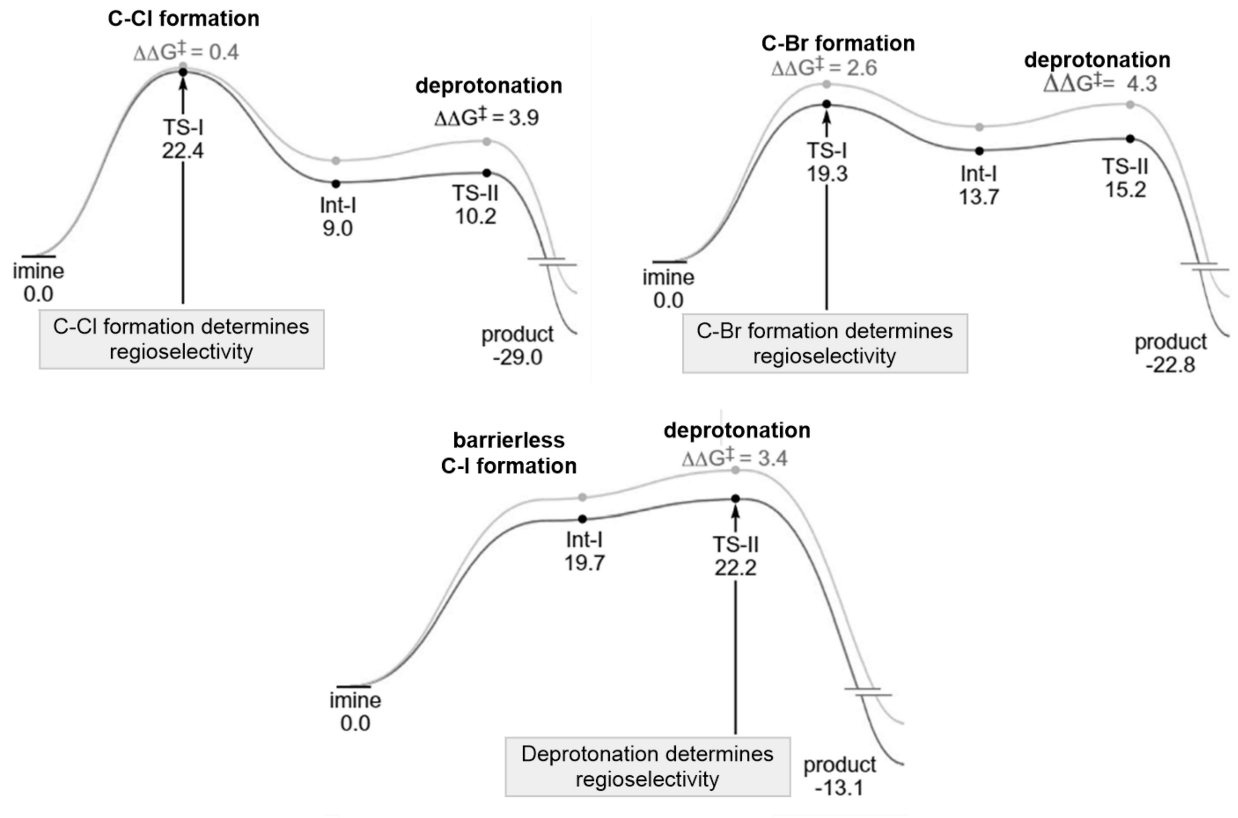

Figure 2.9 Potential energy surfaces for the reaction of *N*-halosuccinimides and 2Ph substituted Zincke Imine.

Calculated free energy surfaces for pyridine and 2Me-substituted pyridine Zincke imines undergoing these halogenation reactions show the selectivity patterns and trends identified align with those observed for the 2-Ph Zincke imine **(Figure 2.10)**.

	TS-I_C3	TS-I_C5	Int-I_C3	Int-I_C5	TS-II_C3	TS-II_C5	Int-II_C3	Int-II_C5
2Me_NIS	N/A	N/A	17.2	20.4	20.1	24.6	-13.6	-6.9
2Me_NBS	17.1	21.3	12.4	17.4	14.9	19.7	-19.9	-16.5
2Me_NCS	22.0	23.4	8.5	12.0	10.2	13.1	-26.8	-23.5
Pyr_NIS	N/A	N/A	23.8	25.3	25.2	27.4	-14.1	-6.4
Pyr_NBS	20.7	N/A	15.9	16.9	17.1	20.1	-21.6	-16.8
Pyr_NCS	25.6	24.9	14.0	15.8	14.6	15.8	-29.8	-23.7

Figure 2.10 Tabulated energies for the reaction of N-halosuccinimides and different imines (2Me Pyridine and Pyridine derivates).

2.3.5 Energy decomposition for Bromination and Chlorination

The most energetically favorable conformation of TS-I in reactions with NBS and NCS on the 2Ph Zincke Imine was analyzed using Energy Decomposition Analysis (EDA) **(Figure 2.11)**. In this analysis, TS-I is deconstructed into its constituents (NXS and Zincke Imine), followed by a single point energy evaluation of the distorted component. $E_{DIST\ NXS}$ represents the energy difference between the ground state NXS and its energy within TS-I. $E_{DIST\ Imine}$ reflects the energy disparity between the ground state Zincke Imine and its energy in TS-I. E_{Int} is the discrepancy between the Activation Energy (E_{Act}) and the cumulative distortion energies of NXS and Imine ($E_{DIST\ NXS}$ + $E_{DIST\ Imine}$). The results indicate that the bromination TS exhibits higher distortion components than chlorination, suggesting its occurrence at a later reaction stage.

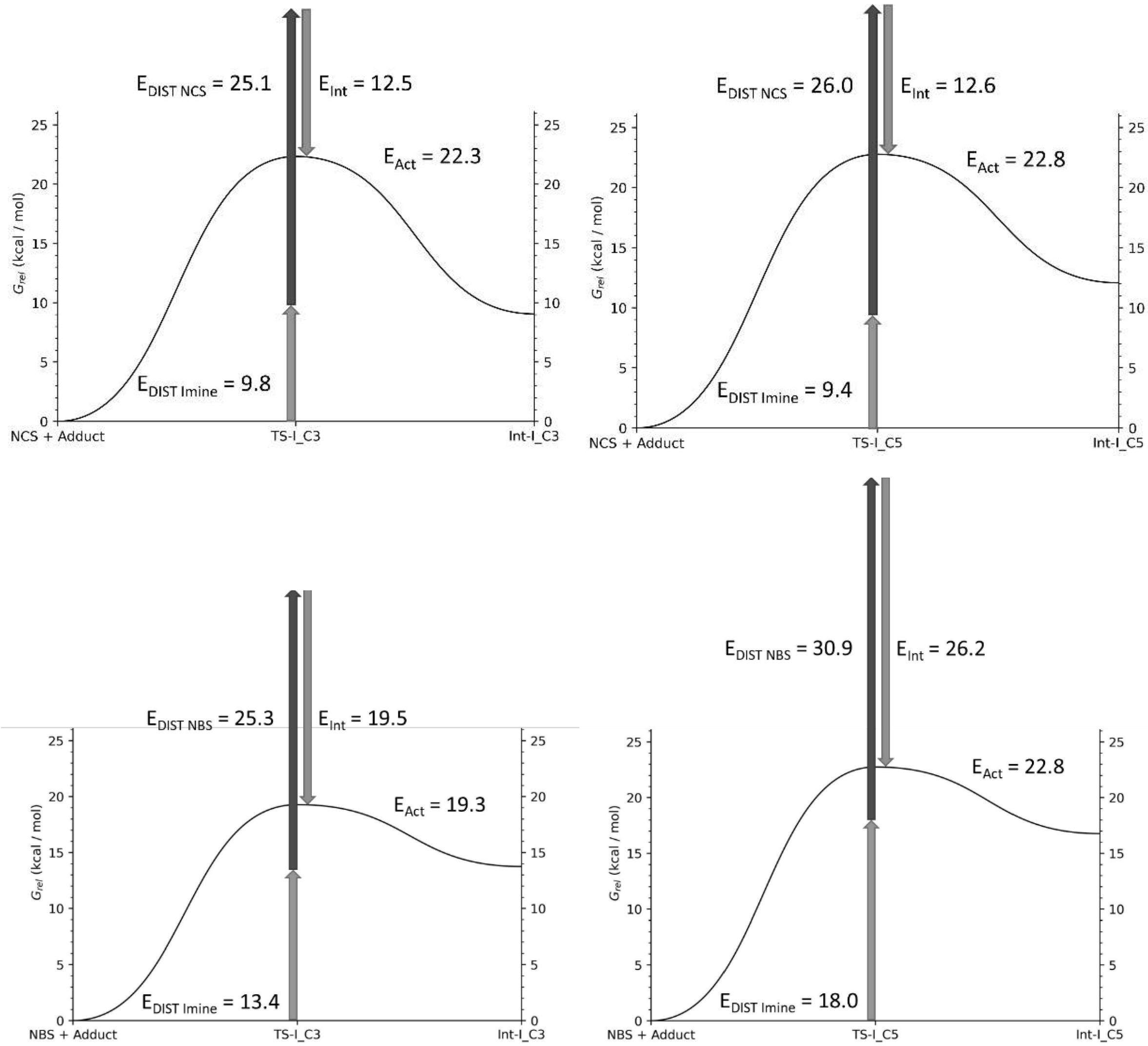

Figure 2.11 Energy decomposition diagrams for the halogenation TSs of the reaction of 2Ph Zincke Imine with NBS and NCS.

Examining the pyramidalization at the carbon being functionalized (C3/C5) **(Figure 2.12)** revealed that the bromination TS is positioned later along the reaction coordinate, with pyramidalization values of 0.76 and 0.80, compared to chlorination, which has pyramidalization values of 0.62 and 0.63. These measurements are relative to the pyramidalization observed at the intermediate succeeding the TS.

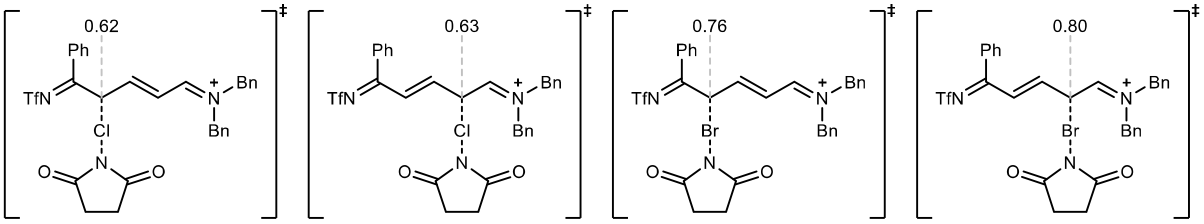

TS-I-C3-NCS TS-I-C5-NCS TS-I-C3-NBS TS-I-C5-NBS

Figure 2.12 Pyramidalization values at the reacting carbon in the halogenation (TS-I). Value shown are relative to pyramidalization at the intermediate following the TS (Int-I).

The greater C3 selectivity observed in bromination compared to chlorination ($\Delta\Delta G^{\ddagger}$ of 2.5 and 0.4 kcal/mol, respectively) is elucidated through the rationale of early versus late transition states (TS). Chlorination leads to a more stable intermediate than bromination, and aligning with the Hammond postulate, proceeds via an earlier TS, as evidenced by reduced TS distortion energies shown in **Figure 2.13** and smaller pyramidalization at the carbon atom undergoing reaction shown in **Figure 2.12**. Due to the electronic similarity between the C3 and C5 positions in Zincke imine and the lack of significant intermolecular non-covalent interactions, there is minimal regioisomeric bias in the early TS for chlorination. Conversely, bromination occurs through a later TS, resulting in more pronounced substrate distortion, which strongly prefers the addition at C3 ($\Delta\Delta E_{dist}$ = 4.6 kcal/mol). This variation in distortion energies suggests a more stable developing α,β-unsaturated iminium ion in TS-I-C3-NBS compared to TS-I-C5-NBS ($\Delta\Delta G^{\ddagger}$ = 2.6 kcal/mol).

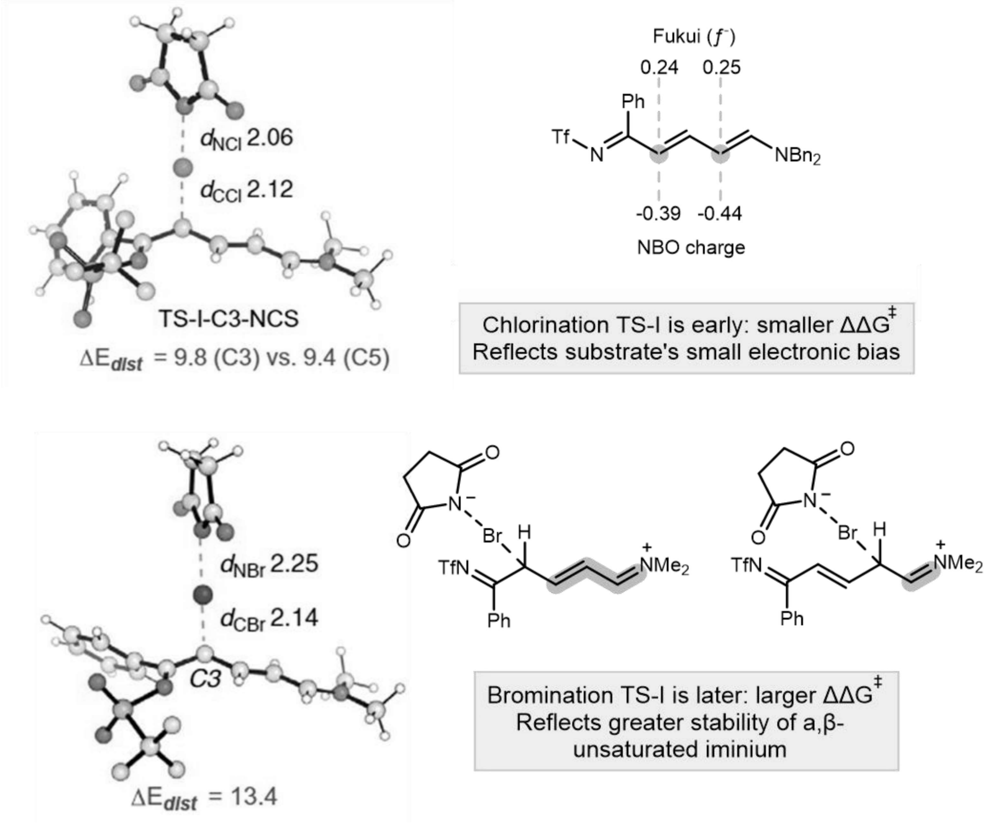

Chlorination TS-I is early: smaller $\Delta\Delta G^‡$
Reflects substrate's small electronic bias

Bromination TS-I is later: larger $\Delta\Delta G^‡$
Reflects greater stability of a,β-unsaturated iminium

Figure 2.13 Rationalization of regioselectivity for NBS and NCS.

2.3.6 Steric and Electronic effects in the deprotonation (TS-II)

To understand the source of selectivity in the iodination reaction which possess a selectivity determining deprotonation, the transition states (TSs) for deprotonation of the 2Ph-Zincke Imine were analyzed **(Figure 2.14)**. Energy barriers of 34.7 and 35.7 kcal/mol were identified for deprotonation at the C3 and C5 positions, respectively, indicating that a significant portion of the selectivity during deprotonation arises from steric interactions between the C5 substituent and the adjacent iminium substituent. The additional selectivity is attributed to the stability conferred by the larger conjugated iminium in the C3 deprotonation.

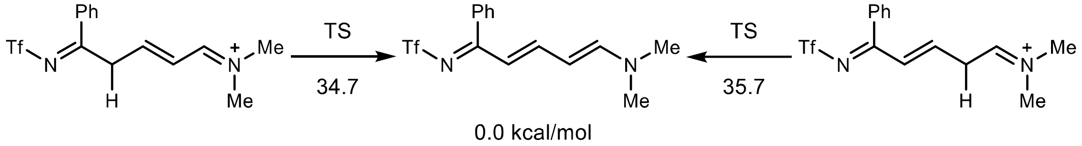

Figure 2.14 Gibbs activation (kcal/mol) for intermolecular deprotonation by the succinimide anion.

This steric interaction is distinctly evident in the geometry of the product (Int-II) **(Figure 2.15)**. For the C3 regioisomer, a bond angle (C2-C3-C4) of 122° is contrasted with a bond angle (C4-C5-C6) of 115° for the C5 regioisomer. The presence of the iminium methyl group also slightly distorts the planarity of the adduct, reflected in the dihedral angles of the conjugated system; 180° (C2-C3-C4-C5) in the C3 regioisomer and 176° (C4-C5-C6-N7) in the C5 regioisomer. Comparable $\Delta\Delta G^{\ddagger}$ values for this step were observed in reactions with NCS and NBS (3.9 and 4.3 kcal/mol, respectively).

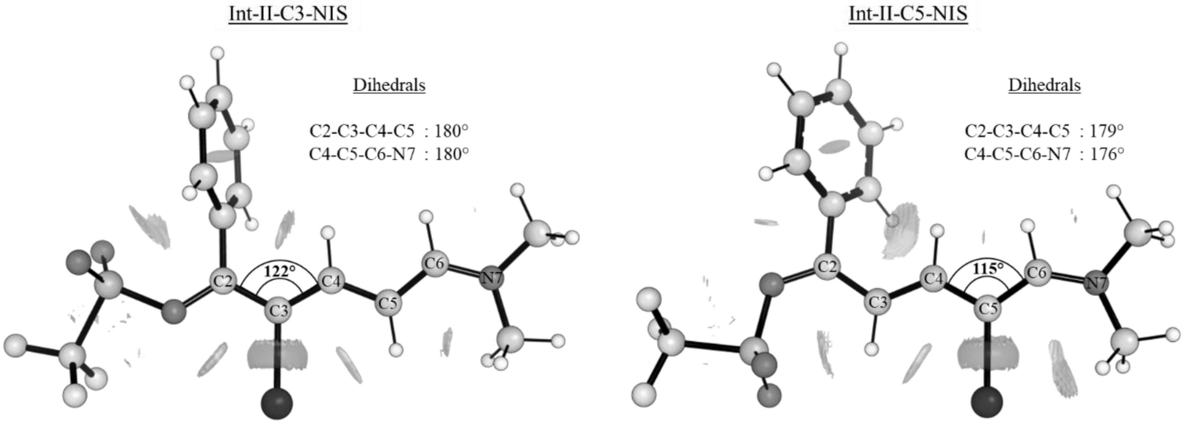

Figure 2.15 Geometry of Int-II in the NIS reaction.

In contrast to bromination and chlorination, the pronounced regioselectivity observed in iodination ($\Delta\Delta G^{\ddagger}$= 3.4 kcal/mol) is due to a rate-limiting and selectivity-determining deprotonation step (TS-II). The restoration of planarity in TS-II-C5-NIS introduces increased $A^{1,3}$

strain between the enamine carbon substituent and the iodide, as illustrated in **Figure 2.16**. The bond and dihedral angles in the product iodinated at C5 showcase the evolving strain **(Figure 2.15)**. Intermolecular competition assays corroborate these theoretical findings. We conducted reactions with equal parts of 2Ph Zincke imine and isotopically labeled [^{2}H]-2Ph Zincke imine until one equivalent of NIS was consumed. The resulting ratio of isotopically labeled S.M. to regular imine is 2.70 at the reaction's conclusion evidences a preferential consumption of non-isotopically labeled imine, affirming the theory-predicted selectivity-determining deprotonation **(Figure 2.16)**. A similar trial with NBS failed to reveal a substantial preference for either the labeled or non-labeled imine, aligning with the prediction that selectivity is determined by the formation of the C–Br bond.

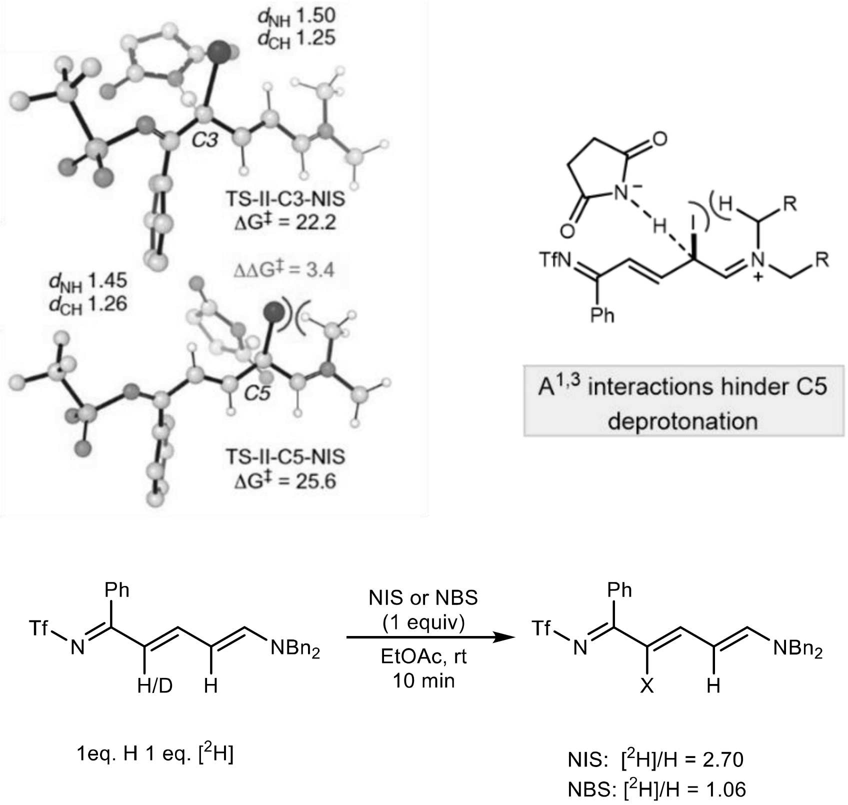

Figure 2.16 Rational for regioselectivity with NIS and intermolecular KIE study.

2.4 Conclusions

This work advances the field of pyridine halogenation by developing an innovative approach centered on the Zincke reaction, particularly emphasizing the conversion of NTf-pyridinium salts into halogenated pyridines. By examining the reactions of Zincke imines with various halogens and leveraging quantum chemical calculations, we elucidated the complex regioselectivity and efficiency of these halogenation processes. The study's findings highlight the crucial roles of electronic and steric factors in determining outcomes, offering insights that align closely with experimental observations.

Significantly, this research provides a versatile methodology for the synthesis of halogenated pyridines, key intermediates in pharmaceutical and agrochemical sectors, through a simplified "one-pot" protocol. This not only addresses previous limitations in the Zincke reaction but also opens new avenues for the efficient and selective synthesis of bioactive compounds. Overall, the contributions of this study offer a foundation for future explorations in organic synthesis, particularly in the development of halogenated organic molecules.

REFERENCES

1. E. Vitaku, D. T. Smith, J. T. Njardarson, J. Med. Chem. 57,10257–10274 (2014).

2. M. Baumann, I. R. Baxendale, Beilstein J. Org. Chem. 9,2265–2319 (2013).

3. V. V. Zakharychev, A. V. Kuzenkov, A. M. Martsynkevich, Chem. Heterocycl. Compd. 56, 1491–1516 (2020).

4. M. Stolar, T. Baumgartner, Chem. Commun. 54,3311–3322 (2018).

5. J. A. Joule, K. Mills, Heterocyclic Chemistry (Wiley, ed. 5, 2009).

6. M. R. Grimmett, Adv. Heterocycl. Chem. 58, 271–345 (1993).

7. K. Murakami, S. Yamada, T. Kaneda, K. Itami, Chem. Rev. 117,9302–9332 (2017).

8. M. L. Crawley, B. M. Trost, Applications of Transition Metal Catalysis in Drug Discovery and Development: An Industria lPerspective (Wiley, 2012).

9. J. F. Bunnett, R. E. Zahler, Chem. Rev. 49, 273–412 (1951).

10. W. F. Bailey, J. J. Patricia, J. Organomet. Chem. 352,1–46 (1988).

11. A. W. Hoffmann, Ber. Dtsch. Chem. Ges. 12, 984–990 (1879).

12. W. J. Sell, F. W. Dootson, J. Chem. Soc. Trans.73, 442–445(1898).

13. W. J. Sell, F. W. Dootson, J. Chem. Soc. Trans.73,432–441 (1898).

14. P. S. Fier, J. F. Hartwig,Science342, 956–960 (2013).

15. G. A. Olah, Acc. Chem. Res.4, 240–248 (1971).

16. B. Galabov, D. Nalbantova, Pv. Schleyer, H. F. Schaefer3rd,Acc.Chem. Res.49, 1191–1199 (2016).

17. S. M. Manolikakes, N. M. Barl, C. Samann, P. Knochel,Z. Naturforsch. B. J. Chem. Sci.68, 411–422 (2013).

18. G. A. El-Hiti, K. Smith, A. S. Hegazy, M. B. Alshammari, A. M. Masmali,ChemInform46, 1 (2015).

19. G. A. El-Hiti, K. Smith, A. S. Hegazy,Heterocycles91, 479–504(2015).

20. M. A. Larsen, J. F. Hartwig, J. Am. Chem. Soc.136, 4287–4299(2014).

21. S. A. Sadleret al.,Org. Biomol. Chem.12, 7318–7327 (2014).

22. J. S. Wright, P. J. H. Scott, P. G. Steel, Angew. Chem. Int. Ed.60, 2796–2821 (2021).

23. L. Yang, N. Uemura, Y. Nakao,J. Am. Chem. Soc.141,7972–7979 (2019).

24. J. Trouvé, P. Zardi, S. Al-Shehimy, T. Roisnel, R. Gramage-Doria, Angew. Chem. Int. Ed.60, 18006–18013 (2021).

25. C. Cheng, J. F. Hartwig, J. Am. Chem. Soc.137,592–595 (2015).

26. X. Y. Zhou, M. Zhang, Z. Liu, J. H. He, X. C. Wang, J. Am. Chem.Soc.144, 14463–14470 (2022).

27. C. D. Vanderwal, J. Org. Chem.76, 9555–9567 (2011).

28. W. C. Cheng, M. J. Kurth, Org. Prep. Proced. Int.34, 585–608(2002).

29. S. Sowmiah, J. M. S. S. Esperanca, L. P. N. Rebelo, C. A. M. Afonso, Org. Chem. Front.5, 453–493 (2018).

30. R. A. Toscano et al. ,Chem. Pharm. Bull.(Tokyo)45,957–961 (1997).

31. J. Becher,Synthesis1980, 589–612 (1980).

32. U. Stämpfli, M. Neuenschwander, Helv. Chim. Acta66,1427–1435 (1983).

33. T. M. Nguyen, M. del Rayo Sanchez-Salvatori, J. C. Wypych, C. Marazano, J. Org. Chem.72, 5916–5919 (2007).

34. A. Tomberg, M. J. Johansson, P. O. Norrby, J. Org. Chem.84,4695–4703 (2019).

35. M. Liljenberg, J. H. Stenlid, T. Brinck, J. Phys. Chem. A122,3270–3279 (2018).

CHAPTER 3: PYRIMIDINE DIVERSIFICATION THROUGH A DECONSTRCUTION-RECONSTRUCTION STRATEGY.

In this chapter is presented the computational work done to elucidate the mechanism of a pyrimidine transformation in order to understand and expand the limitations of the original method.

This work is the result of a collaboration with Benjamin Uhlenbruck and Celena Josephitis from Andrew McNally's research group. All experimental work was performed by B.U. and C.J. all calculations were performed by L.d.L. This work was accepted as "A Deconstruction-Reconstruction Strategy for Pyrimidine Diversification" in *Nature* (2024).

3.1 Background and significance

3.1.1 Molecular Editing as an SAR strategy

Modifying the structure of candidate compounds in Structure-Activity Relationship (SAR) studies enables the optimization of their physiochemical properties in drug and agrochemical development.[1] Practitioners commonly select portions of a candidate's structure to diversify during these studies, and altering the periphery of azines, such as pyrimidines, is frequently employed because they are pervasive and often form key binding interactions with the biological target.[2-5] Rapid access to analog compounds is paramount; therefore, chemical reactions that make structural modifications in one or two steps are valuable, particularly during later stages of development involving complex structures.[6,7] Although many individual reactions can transform azines, they typically fall within only two effective strategies, transforming embedded functional groups and C–H functionalization reactions, that enable rapid diversification for SAR studies.[8] Molecular editing is emerging to produce analog compounds for SAR studies but is typically associated with transforming one candidate compound to a single derivative.[9] We reasoned that deconstructing complex pyrimidines to a parent synthetic intermediate, with a large set of associated chemical reactions, could expand this strategy. In this way, reconstructing substituted versions of the original pyrimidine and accessing other heterocycles becomes viable through simple cyclization reactions. This approach both diversifies a candidate's structure and can generate chemical libraries, making it a potentially useful tactic in SAR studies.[10]

3.1.2 De novo heterocycle synthesis

The de novo synthesis of heterocycles involves the cyclization of smaller molecular fragments into substituted rings, a notable example being the use of 1,3-dicarbonyl compounds to generate substituted azines and azoles.[1,11] This method is frequently applied in creating fundamental building blocks like pyrimidines, pyrazoles, and 1,2-oxazoles. Techniques for fragment coupling, such as those used to synthesize the aminopyrimidine core in gleevec, also employ de novo synthesis, generating extensive libraries thanks to the readily available starting materials such as amidines and hydrazines **(Figure 3.1)**.[12,13] Although this approach is advantageous in the early stages of drug discovery, it becomes progressively less effective for SAR analysis on complex molecular architectures. The strategy of maintaining heterocycle precursors, like 1,3-dicarbonyls or their analogs, across numerous synthetic steps and then diversifying them in the latter phases is often impractical due to their propensity to interact with a wide range of organic compounds and reagents. Consequently, developers typically advance building block heterocycles through several stages of synthesis to produce analog compounds. Given that critical heterocycles are already present in advanced drug candidates, the de novo methodology seems less appropriate for detailed SAR investigations. However, we have devised a strategy that transforms complex pyrimidine-containing structures into iminoenamines, surrogates of 1,3-dicarbonyl compounds, and then leverages de novo heterocycle synthesis to obtain substituted pyrimidine and 1,2-azole analogs. This way, practitioners can envisage a masked, diversifiable three-carbon unit within pyrimidines and strategize for late-stage SAR applications.

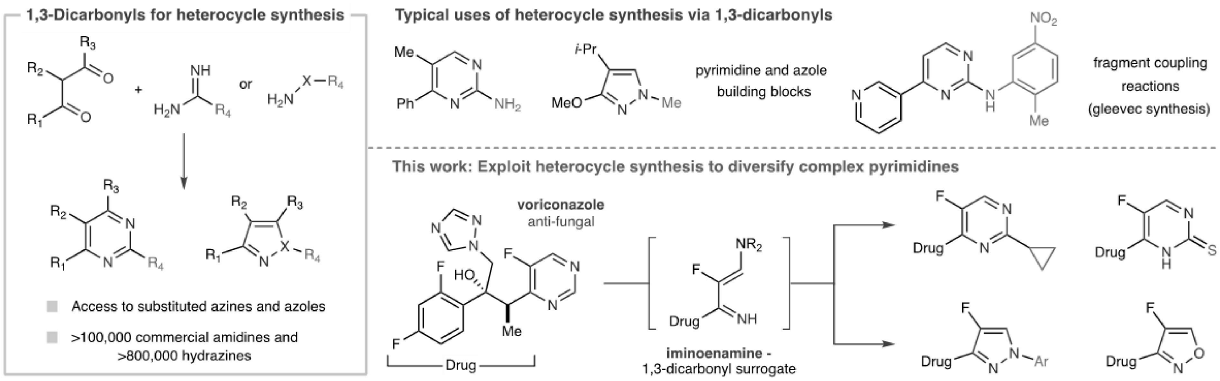

Figure 3.1 de novo synthesis of heterocycles from pyrimidines through iminoenamine intermediates.

3.2 Experimental findings

This novel method leverages de novo synthesis of heterocycles, inspired by an unexpected result depicted in **Figure 3.2**. Our team has previously shown that pyridines, when treated with Tf_2O and dibenzylamine, undergo transformation into ring-opened Zincke imines, which can then be halogenated and reformed into 3-halopyridines.[14] In an attempt with 4-phenylpyrimidine and aniline acting as the nucleophile,[15] instead of forming the anticipated ring-opened aza-Zincke imine, we surprisingly produced N-phenyl pyrimidinium salt in significant yield.[16] Subsequently, the removal of the C2 carbon atom was achieved with ethanolic piperidine, yielding predominantly the iminoenamine and a smaller quantity of a vinamidinium salt, as determined by the preliminary ^{1}H NMR spectra using an internal standard. Iminoenamines, derivatives of 1,3-dicarbonyl compounds, are crucial precursors for the de novo creation of heterocycles. As illustrated in **Figure 3.1**, recyclization in situ with guanidine in a basic setting led to the formation of 2-aminopyrimidine with favorable yield. Furthermore, introducing hydroxylamine and hydrochloric acid to the raw mix containing the iminoenamine yielded 1,2-oxazole as regioisomeric mixtures. Such 'scaffold hopping' techniques have recently come to prominence within the rapidly evolving field of molecular editing.[17-23] Sarpong has documented that hydrazines, when reacted with NTf-pyrimidinium salts, lead to the formation of pyrazoles through a sequence of ring-opening and ring-closing reactions.[24] This approach allows for the generation of multiple heterocyclic frameworks from iminoenamines, rather than a straightforward one-to-one structural transformation.[25] Our initial study effectively validates the concept of applying de novo synthesis to existing heterocycles; the next stage is to evaluate its applicability across a range of pyrimidine substrates and cyclization agents.

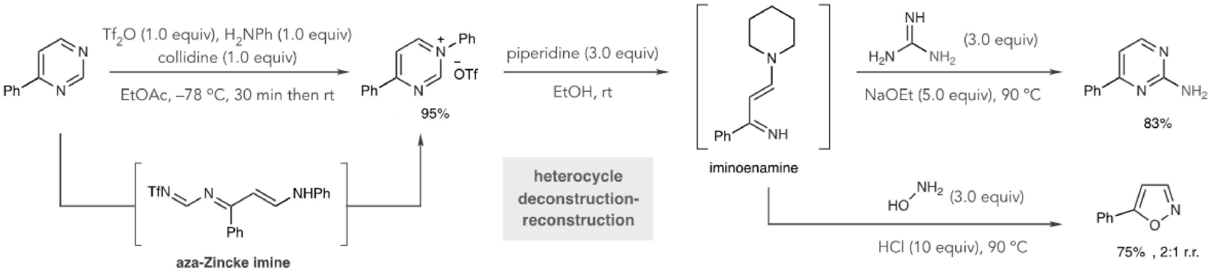

Figure 3.2 Experimental conditions for pyrimidine to pyrimidinium transformation and subsequent cleavage and condensation.

3.3 Computational findings

3.2.1 Free energy surface for main reaction

In the mechanistic part of this project, we studied the mechanism of N-arylpyrimidinium salt formation computationally by performing quantum chemical calculations at the ωB97X-D/def2-TZVP//ωB97X-D/6-31+G(d,p) level of theory, with an SMD description of ethyl acetate. **Figure 3.3** shows the computed potential energy surface for the reaction of 4-phenyl pyrimidine with Tf_2O and aniline.

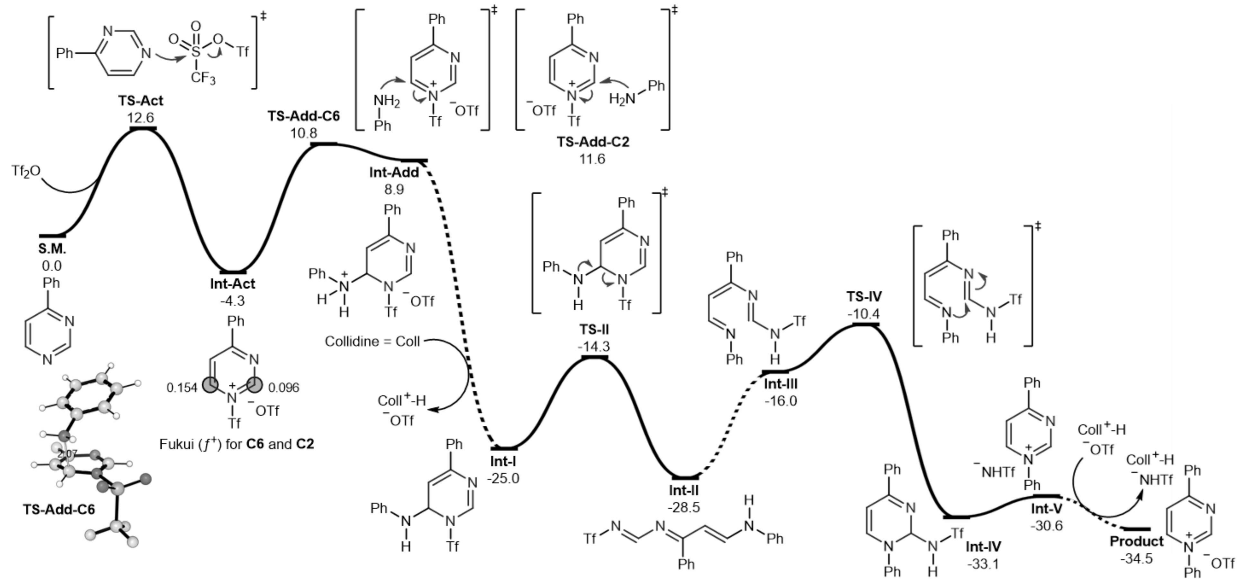

Figure 3.3 Free energy surface for the reaction of 4-phenyl pyrimidine, triflic anhydride, collidine and aniline reacting at the C6 of the pyrimidinium.

The reaction between 4-Ph pyrimidine and Tf_2O is exergonic (–4.3 kcal mol^{-1}) and proceeds in a single step via TS-Act ($\Delta G^{\ddagger}$ 12.6 kcal mol^{-1}). Aniline then adds to the resulting NTf-pyrimidinium with nucleophilic attack at C6 ($\Delta G^{\ddagger}$ 15.1 kcal mol-1 via TS-Add-C6) preferred over

C2 ($\Delta G^{\ddagger}$ 15.9 kcal mol^{-1} via TS-Add-C2), which corresponds to a kinetic selectivity of 8:1 at –78 ºC. These transition structure (TS) energies reflect the electronic Fukui (f +) indices that indicate greater electrophilicity at C6 vs. C2 (0.15 vs. 0.10). Although the C6-adduct formed in endergonic by 8.9 kcal mol^{-1}, deprotonation of the ammonium species by collidine occurs in an energetically barrierless process to produce a stable intermediate, Int-I (ΔG –20.7 kcal mol^{-1}) and indicates that the base drives this process forward.

Next, Int-I undergoes facile ring-opening ($\Delta G^{\ddagger}$ 10.7 kcal mol^{-1} via TS-II) to form aza-Zincke imine Int-II (shown in its most stable E, Z, E configuration), which is thermodynamically favored by 3.5 kcal mol^{-1}. Int-II then tautomerizes and isomerizes to Int-III before ring-closing via TS-IV ($\Delta G^{\ddagger}$ 18.1 kcal mol^{-1}, relative to Int-II) to form dihydropyrimidine derivative Int-IV in exergonic fashion (ΔG –4.6 kcal mol^{-1}). Ring closure is the largest barrier along the reaction coordinate, making TS-IV rate-limiting. Ejection of a triflamide anion yields a stable ion pair (Int-V), and subsequent anion metathesis results in the pyrimidinium triflate 3a (overall $\Delta G^{\ddagger}$ –34.5 kcal mol^{-1}).

Alternatively, addition at the C2 **(Figure 3.3)** yields Int-I at -24.2 kcal mol^{-1} which undergoes ring opening with a lower barrier of 5.6 kcal compared to it’s C6 isomer. This ring opening yield Int-II at -29.2 kcal mol^{-1}. The barrier for ring closing is significantly higher for this isomer than for the C6 with a barrier of 26.8 kcal mol^{-1} vs 18.1 kcal mol^{-1} for the C6. We further explored this phenomenon.

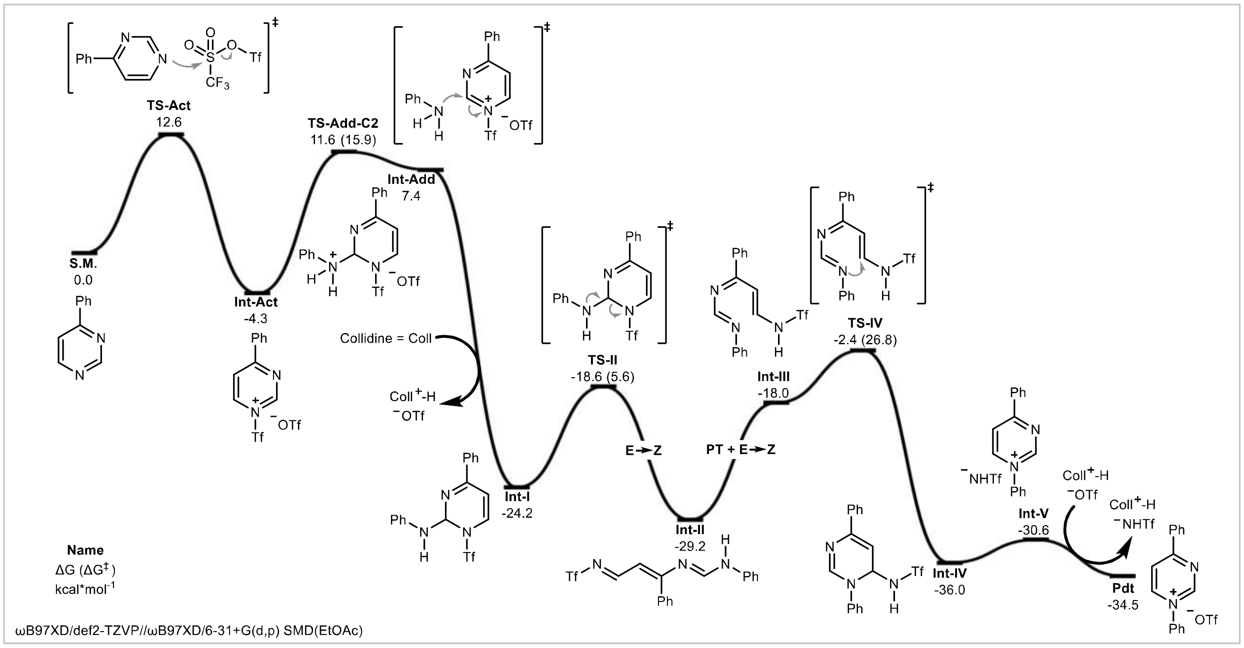

Figure 3.3 Free energy surface for the reaction of 4-phenyl pyrimidine, triflic anhydride, collidine and aniline reacting at the C2 of the pyrimidinium.

3.2.2 NICS calculations

We performed Nucleus Independent Chemical Shift calculations (NICS(0)$_{zz}$, B3LYP/6-311+G(d,p) level of theory) at the ring center of each ring-opening and ring-closing TS, to investigate whether these structures exhibit aromatic shielding patterns characteristic of pericyclic transformations **(Figure 3.4)**.[37] These calculations gave positive values of 8.6 and 8.0 ppm for TS-II and TS-IV, respectively. For context, the transition structure for the 6π-electrocyclization of 1,3,5-hexatriene has a NICS(0)$_{zz}$ value of –29.5 ppm and a barrier of 33.1 kcal mol^{-1} at the same level of theory. Thus, since no aromaticity is found in these TSs, they describe polar processes rather than electrocyclic reactions. These polar reactions have relatively low barriers, may be considered as pseudo-pericyclic, and can proceed at much lower temperatures.[38,39] For the minor regioisomer, corresponding to aniline adding at C2, the ring-closing barrier is raised significantly by 8.5 kcal mol^{-1} relative to the major regioisomeric pathway shown. Interestingly, the ring-closing TS for this minor pathway shows a lower NICS(0)$_{zz}$ value (4.5 ppm), consistent with less polar (and greater pericyclic) character.

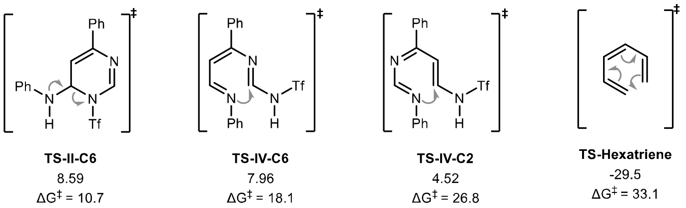

Figure 3.4 NICS calculations for ring opening and ring closing reactions.

3.2.3 Free energy surface for 4-Alkyl and 4-Ester substrates

To computationally investigate the scope of the reaction we also modelled the reaction with a 4-Me and 4-CO2Me substrate. The reaction is not amenable to 4-alkyl substrates where alkyl is a primary or secondary group and is lower yielding for 4-EWG substrates such as 4 esters.

Reaction with 4-Me pyrimidine **(Figure 3.5, Figure 3.6)** appears to favor reactivity at the C2 position with TS-Add-C2 at 14.3 kcal mol^{-1} against TS-Add-C2 with a barrier of 15.1 kcal mol^{-1}. This is in contrast with the 4 -phenyl pyrimidine which favored addition at the C2. This addition yields, after ring opening, Int-II at -29 kcal mol^{-1} ,this intermediate has a high barrier to ring close (TS-IV at 29.8 kcal mol^{-1}) due to the lesser polarity of the transition state. The energies of the two intermediates Int-II for the C2 and C6 are very close in energy indicating that this effect is not ground state destabilization but TS destabilization. This effect observed with all substitutions patterns and described in the previous chapter through a study of the aromaticity of the TSs. Because of this we believe that the regioselectivity of the initial addition is crucial to the success of the reaction. Alternatively, we also believe that 4-alkyl pyrimidiniums are prone to deprotonation at the alkyl proton which could lead to decomposition of the starting material.

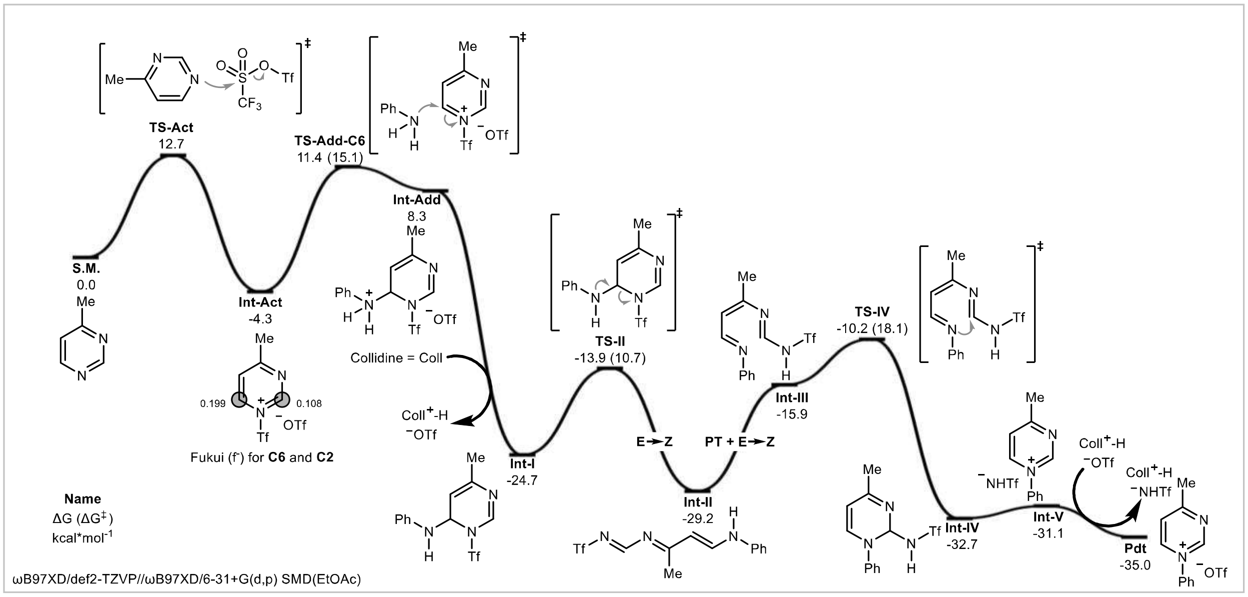

Figure 3.5 Free energy surface for the reaction of 4-methyl pyrimidine, triflic anhydride, collidine and aniline reacting at the C6 of the pyrimidinium.

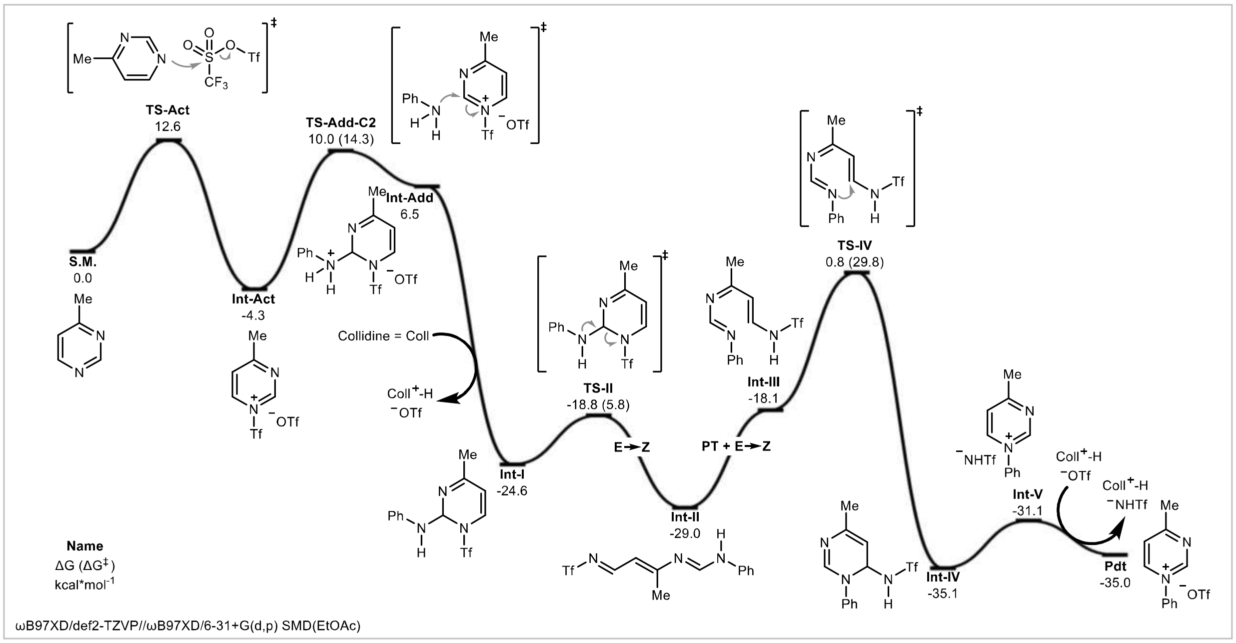

Figure 3.6 Free energy surface for the reaction of 4-methyl pyrimidine, triflic anhydride, collidine and aniline reacting at the C2 of the pyrimidinium.

Reaction with the 4-CO_2Me pyrimidine **(Figure 3.7, Figure 3.8)** appears to proceed at the C6 position with a barrier of 15.3 kcal mol^{-1} favored over addition at C2 (16.9 kcal mol^{-1}). This yields, after ring opening, Int-II at -27.1 kcal mol^{-1}. Follows ring closing with a barrier of 16.5 kcal mol^{-1} slightly lower than for the 4-Phenyl substrate. This ester substrate possesses a much higher barrier of activation (TS-Act) at 16.6 kcal mol^{-1} versus 12.6 kcal mol^{-1} for the phenyl substrate. We believe competition for triflylation with aniline is responsible for the poor performance of this substrate.

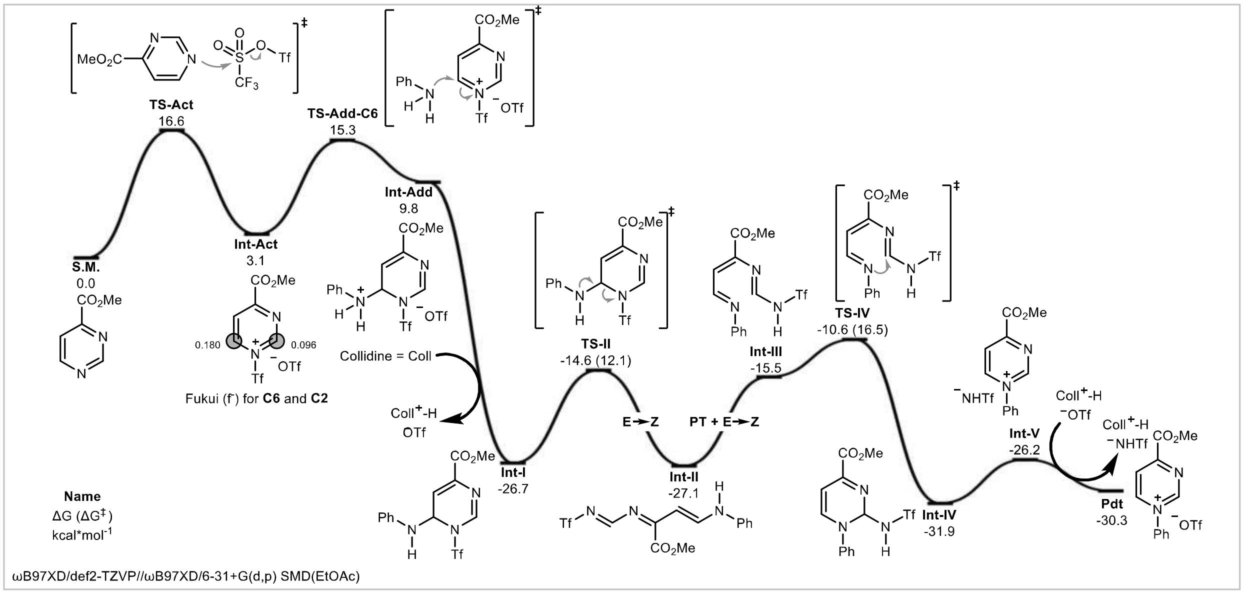

Figure 3.7 Free energy surface for the reaction of 4-CO_2Me pyrimidine, triflic anhydride, collidine and aniline reacting at the C6 of the pyrimidinium.

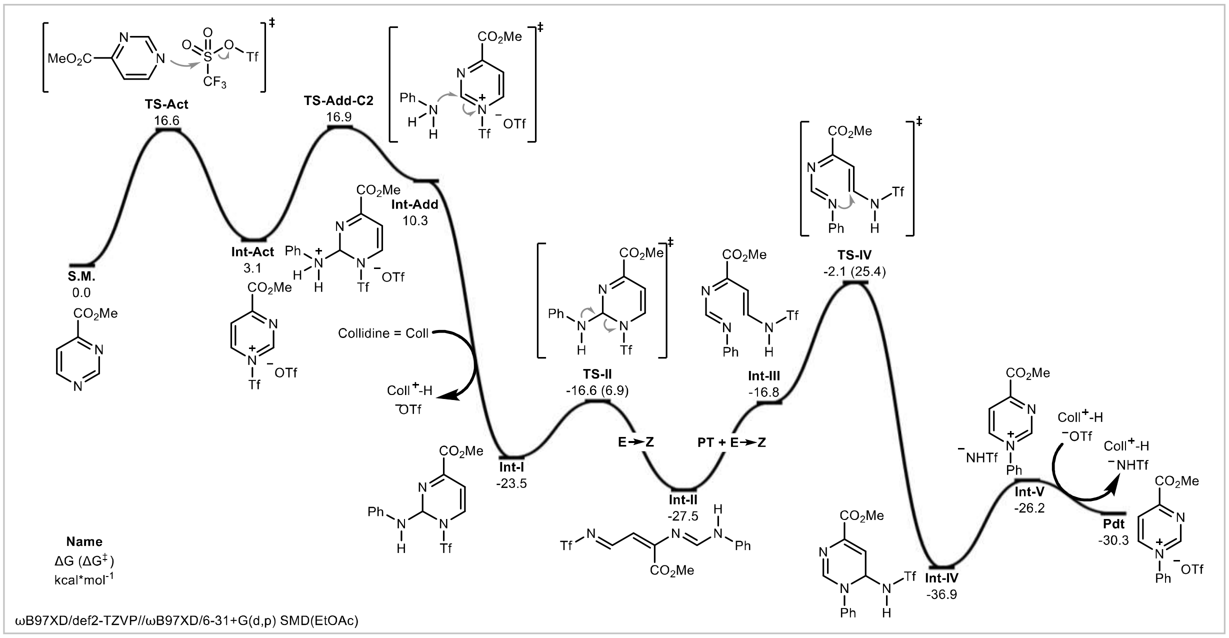

Figure 3.8 Free energy surface for the reaction of 4-CO_2Me pyrimidine, triflic anhydride, collidine and aniline reacting at the C2 of the pyrimidinium.

3.2.4 Alternative triflylation reactions

To discern which species might be competing for reaction with triflic anhydride, we examined the thermodynamic and kinetic attributes of various triflylation reactions with the species present in solution the results are shown in **Figure 3.9**. The triflylation of collidine appeared improbable, having a significant activation barrier of 18.3 kcal mol^{-1} and being marginally exothermic at -0.7 kcal mol^{-1}.

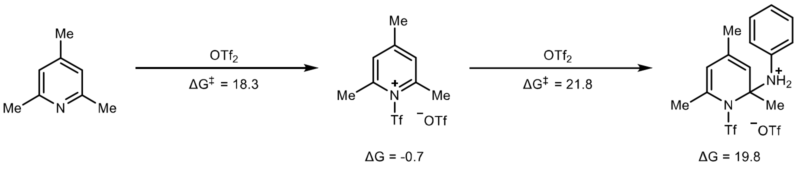

Figure 3.9 Reaction of collidine, triflic anhydride and aniline.

Next, we investigated the triflylation of the triflimide anion, which is formed in the initial reaction **(Figure 3.10)**. This reaction was found to be markedly exergonic, with a change in energy of -28.3 kcal mol^{-1} and displayed competitive kinetics for triflylation of the 4-ester pyrimidine, presenting an activation barrier of 17.2 kcal mol^{-1}.

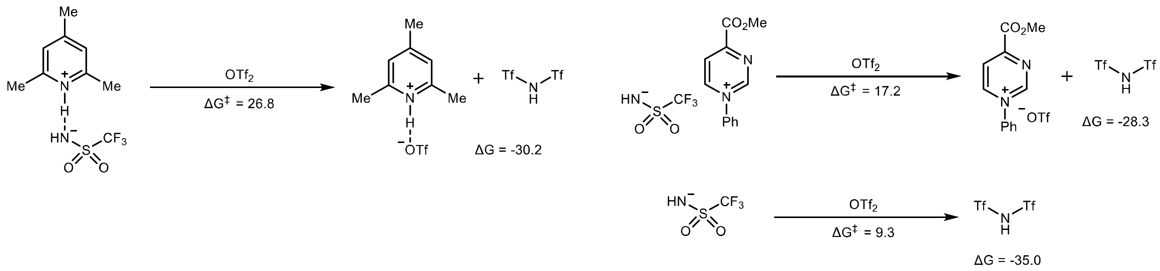

Figure 3.10 Triflylation reaction of different salt forms and naked triflimide anions.

Our inquiry extended to whether aniline was subject to triflylation **(Figure 3.11)**. It emerged that aniline could indeed outperform our electron-deficient pyrimidines, with a lower activation barrier of 15.8 kcal mol^{-1}. Electron-deficient anilines exhibit higher barriers to triflylation and lack sufficient nucleophilicity to engage at the pyrimidine (TS-Add-C6), with *p*-NO2 anilines showing an addition barrier ranging from 22.6 to 23.2 kcal mol^{-1}. We noted that bulky anilines, like *o*-tBu aniline, presented a greater triflylation barrier (17.2 kcal mol^{-1}) yet maintained lower addition barriers (14.9 kcal mol^{-1}). This suggests that the triflylation reaction is more affected by steric hindrance due to greater substitution at the sulfur center.

Anilines	TS-Triflylation	TS-Addition-C6
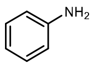	15.8	15.3
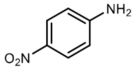	22.0	22.6
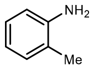	15.0	15.5
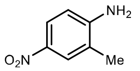	22.0	23.2
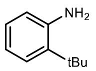	17.2	14.9

Figure 3.11 Triflylation and addition to C6 of N-Tf pyrimidinium TS free energies of different anilines.

3.2.5 Substituents effect on cyclization barrier

Our computation studies indicate that the pyrimidine substituents' size and electronic properties significantly impact the energy barriers for product formation. We described the effect of 14 different C4-substituents on the barrier for ring-closure (TS-IV) using a bivariate linear regression model featuring tabulated A-values and Hammett σ_p constants **(Figure 3.12)**. In the aza-Zincke imine intermediates (e.g., Int-II), groups at the 4-position experience destabilizing steric interactions through $A^{1,3}$ strain relative to the cyclic geometry in TS-IV. Ring-closing barriers, therefore, decrease in response to increasing ground state destabilization caused by larger 4-substituents, as exemplified by 4-phenyl pyrimidine ($\Delta G^{\ddagger}$ = 18.1 kcal mol^{-1}) and 4-methylpyrimidine ($\Delta G^{\ddagger}$ 18.0 kcal mol^{-1}) relative to pyrimidine ($\Delta G^{\ddagger}$ 22.7 kcal mol^{-1}). Electronic effects at the 4-position are also apparent due to conjugation with two imine-like carbons; electron-withdrawing groups, such as trifluoromethyl, further destabilize Int-II, lowering the cyclization barrier ($\Delta G^{\ddagger}$ 12.7 kcal mol^{-1}). Although a 4-CO_2Me group has a relatively low TS-IV barrier ($\Delta G^{\ddagger}$ 16.5 kcal mol^{-1}), we observed moderate yield when transforming 4-CO_2Et pyrimidine into its pyrimidinium salt.

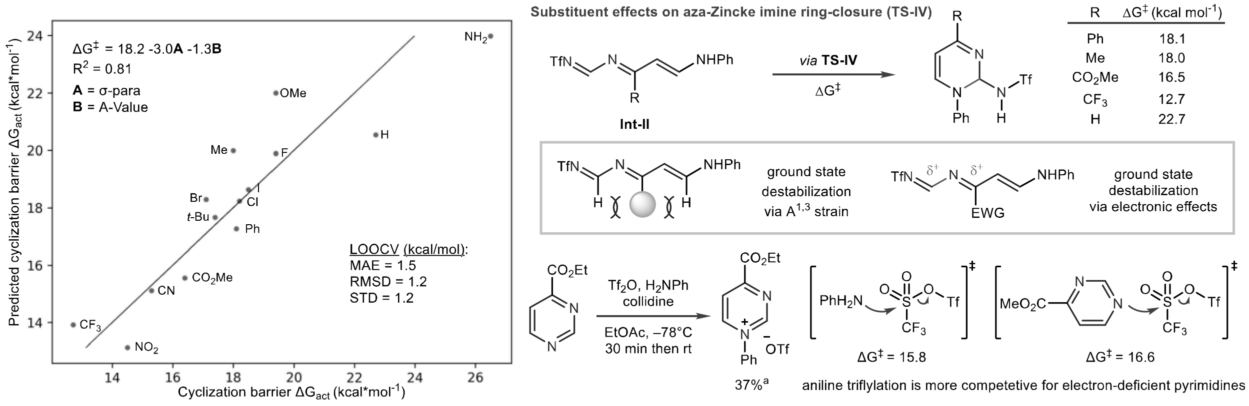

Figure 3.12 Rationalization for the effect of pyrimidine substitution on the success of the reaction.

3.4 Conclusion

In summary, we have shown an alternative approach for pyrimidines diversification by transforming their *N*-arylpyrimidinium salts into iminoenamines and exploiting heterocycle-forming reactions to obtain substituted 2-substituted pyrimidines and 1,2-azoles. This deconstruction-reconstruction approach functions on complex structures and enables de novo heterocycle synthesis as a tactic for late-stage functionalization. Computational studies revealed the size and electronic properties of the pyrimidines' substituents impact ring-closing in the salt-forming stage. Additionally, we found that the regioselectivity of the initial nucleophile addition is crucial to reaction success and identified competing triflylation reactions which we addressed by tailoring the aniline to prevent triflylation but still allow addition at the pyrimidine. Moreover, we demonstrated that other heterocycles, such as pyridines, are accessible via this approach. This deconstruction-reconstruction strategy will extend to heterocycle classes beyond pyrimidines.

REFERENCES

1. J. A. Joule, K. Mills, *Heterocyclic Chemistry*. 5th edn, (Wiley, 2009).

2. M. Baumann, I. R. Baxendale, *Beilstein J. Org. Chem.* 9, 2265-2319 (2013).

3. E. Vitaku,, D. T. Smith, J. T. Njardarson, *J. Med. Chem.* 57, 10257-10274 (2014).

4. Bhutani, P. *et al. J. Med. Chem.* 64, 2339-2381 (2021).

5. Nadar, S. Khan, T. *Chem. Biol. Drug. Des.* 100, 818-842 (2022).

6. Cernak, T., Dykstra, K. D., Tyagarajan, S., Vachal, P. Krska, S. W. *Chem. Soc. Rev.* 45, 546-576 (2016).

7. L. Zhang, T. Ritter, *J. Am. Chem. Soc.* 144, 2399-2414 (2022).

8. C. M. Josephitis , H. M. H. Nguyen, , *A.* McNally, *Chem. Rev.* 123, 7655-7691 (2023).

9. J. Jurczyk, et al. *Nat. Synth.* 1, 352-364 (2022).

10. D. C. Blakemore et al. *Nat. Chem.* 10, 383-394 (2018).

11. J. J. Li, E. J. Corey, *Name Reactions in Heterocyclic Chemistry II.* (Wiley, 2011).

12. Y. F. Liu *et al. Org. Process Res. Dev.* 12, 490-495 (2008).

13. CAS Scifinder^n database search for commercial fragments Novermber 2023: amidines 178,649, hydrazines - 830,858.

14. B. T. Boyle, J. N.Levy , L. de Lescure , R. S. Paton, A. McNally, *Science* 378, 773-779 (2022).

15. J. D. Selingo *et al. J. Am. Chem. Soc.* 146, 936-945 (2023).

16. G. L. Bartholomew, *et al. J. Am. Chem. Soc.* 146, 2950-2958 (2024).

17. P. Barczynski, H.C. Vanderplas, *J. Org. Chem.* 47, 1077-1080 (1982).

18. Y. Hu, D. Stumpfe, J. Bajorath, *J. Med. Chem.* 60, 1238-1246 (2017).

19. C. Lamberth, *Pest. Manag. Sci.* 74, 282-292 (2018).

20. J. Woo *et al Science* 376, 527-532 (2022).

21. B. D. Dherange, P. Q. Kelly, J. P. Liles, M. S. Sigman, M. D. Levin, *J. Am. Chem. Soc.* 143, 11337-11344 (2021).

22. J. C. Reisenbauer, O. Green, A. Franchino, P. Finkelstein, B. Morandi, *Science* 377, 1104-1109 (2022).

23. S. C. Patel, N. Z. Burns, *J. Am. Chem. Soc.* 144, 17797-17802 (2022).

24. G. L. Bartholomew, F. Carpaneto, R. Sarpong, *J. Am. Chem. Soc.* 144, 22309-22315 (2022).

25. N. Nishiwaki, T. Ogihara, T. Takami, M. Tamura, M. Ariga, *J. Org. Chem.* 69, 8382-8386 (2004).

CHAPTER 4: HOMOLOGATION OF ELECTRON-RICH BENZYL BROMIDE DERIVATIVES VIA DIAZO C-C BOND INSERTION.

In this chapter is presented the computational work done to elucidate the selectivity and mechanism of a C-C bond insertion reaction going through phenonium ions intermediates.

This work is a collaboration with Atanu Modak and Kathryn J. Rynders from Nicholas J. Race's research group and Juan V. Alegre-Requena in Robert Paton's research group. All experimental work was performed by A.M. and K. J. R. calculations were performed by J. V. A-R and L.d.L. This work was published as "Homologation of Electron-Rich Benzyl Bromide Derivatives via Diazo C-C Bond Insertion" in *J. Am. Chem. Soc.* (144, 1, 86-92, 2022).

4.1 Background and significance

Synthetic methodologies for organic compounds often rely on the interplay between nucleophiles and electrophiles.[1] For instance, derivatives of benzyl halide can engage in traditional reactions like nucleophilic substitution and electrophilic aromatic substitution.[2] The emergence of techniques that enable "nontraditional" transformations of standard building blocks opens new pathways to either reimagine or streamline synthetic approaches. Such "nontraditional" reactions are characterized by their occurrence at typically unreactive sites, such as insertion into the $C(sp^2)-C(sp^3)$ bond of a benzyl halide derivative. Employing cascade reactions that achieve formal C−C bond insertions through structural rearrangements offers a promising strategy toward this end.[3,4] In this context, we introduce a homologation reaction for electron-rich benzyl bromide derivatives that achieves the formal insertion of diazo compounds into the $C(sp^2)-C(sp^3)$ bond.[5]

Aware of the ionic interactions between diazo compounds and sp^2-hybridized electrophiles, such as carbonyl groups,[6] we explored the potential reaction of electron-rich benzyl bromide with diazo compound. We hypothesized that this could proceed through the formation of a stabilized benzylic carbocation, leading to alkyl diazonium ion **(Figure 4.1)**.[7] Subsequent nitrogen loss could then initiate aryl ring participation, forming the phenonium ion.[8,9] The initial bromide leaving group might then interact with the nascent spirocyclopropane at its less substituted position, yielding the targeted product.[10] We also considered the formation of a tertiary bromide as a possible side product, which could arise either through competitive nitrogen displacement in the diazonium or through nucleophilic attack on the phenonium ion at a more substituted site. The target product features an acyclic, benzylic tertiary or quaternary center, motifs common in numerous pharmaceutical and agrochemical compounds[11,12] ,while preserving the alkyl bromide for further functionalization.[13,14] This technique offers a unified approach for incorporating various functional groups, including trifluoromethyl, ester, amide, ketone, and sulfone groups. The inclusion of trifluoromethyl groups remains a key strategy in medicinal chemistry,[15] with the application of trifluoromethyl-substituted diazo compounds being notably underutilized in this area.[16]

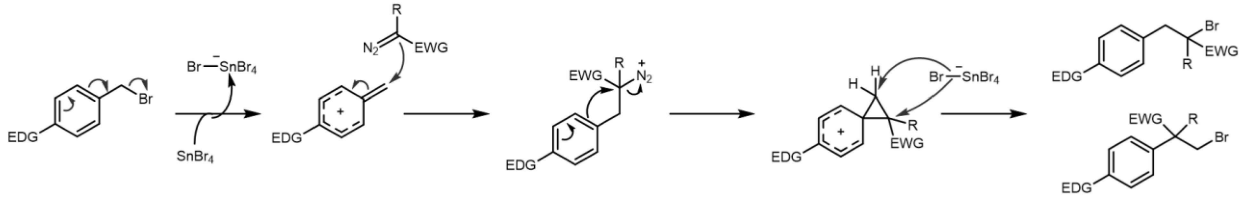

Figure 4.1 Proposed mechanism for nonclassical insertion of diazo compounds into C-C bond of benzyl bromide derivatives.

4.2 Experimental findings

For initial experimentation and optimization, 4-methoxybenzyl bromide and trifluoromethyl diazo were selected. Investigation across a range of Lewis acids and conditions revealed that $SnBr_4$ (50 mol%) in CH_2Cl_2 at -78°C yielded the desired bromide product with a 75% isolated yield. Once optimized, the reaction's scope was assessed for different diazo and benzyl bromide variants. Various electron-withdrawing groups on the diazo component were successfully incorporated. Diazo derivatives with an ethyl ester, benzyl ester, redox-active ester, and a nitrile all participated effectively. With ester derivatives, minor amounts of unwanted isomer were detected in the ^1H NMR of the crude mix. The use of monosubstituted diazo compounds to create tertiary benzylic centers also demonstrated the versatility of electron-withdrawing substituents in this methodology, yielding products with ethyl ester, benzyl ester, tert-butyl ester, amide, ketone, trifluoromethyl group, and a sulfone, all confirming the method's efficacy in synthesizing desired tertiary benzylic centers.

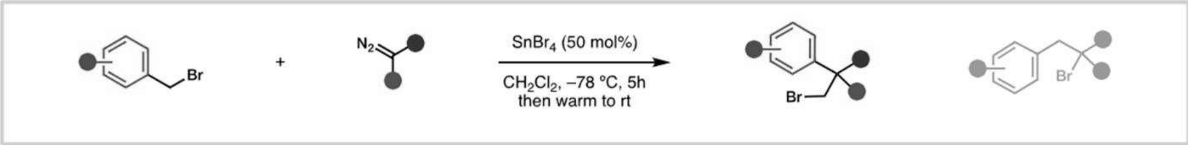

Figure 4.2 Reaction conditions used to achieve desired transformation.

4.3 Computational findings

4.3.1 Methods

Quantum chemical studies employing the ωB97X-D/def2-QZVPP//ωB97X-D/6-31+G(d,p) level of theory, complemented with an SMD solvation model for dichloromethane, were conducted to dissect the multistep reaction mechanism and the source of product selectivity between 4-methoxybenzyl bromide and benzyl 2-diazobutanoate (serving as a model compound) in the presence of SnBr4 catalyst **(Figure 4.3)**.[17]

4.3.2 Potential energy surface

The initial step, leading to the formation of intermediate Int-II, is calculated to favor an S_N1 mechanism with an activation barrier of 18.5 kcal/mol for TS-II, compared to 29.7 kcal/mol for an uncatalyzed S_N2 pathway. This step is identified as the rate-limiting step, where electron-rich benzyl bromide derivatives present lower activation barriers. The coordination between the bromide and the Lewis acid facilitates the formation of a $SnBr_5^-$ leaving group in TS-I. Crossing TS-II initiates a sequence where dinitrogen is lost, and phenonium ion is formed through distinct C−N cleavage (TS-III) and C−C bond formation (TS-IV) transition states, leading to a highly exergonic release of energy (G_{rel} = −32.3 kcal/mol) to yield phenonium Int-IV. The reaction pathway features intermediate states, alkyl diazonium Int-II and tertiary carbocation Int-III, as local energy minima with negligible exit barriers of merely 0.3 and 2.0 kcal/mol, respectively. In contrast, competing 1,2-hydride shifts (TS-VI and TS-VII) present slightly higher barriers, between 3.4 and 3.6 kcal/mol. Given these minimal barrier heights, Int-II and Int-III are anticipated to be transient, potentially precluding the equilibrium of atomic motions and solvent interactions, thus limiting the relevance of transition state theory (TST)[18]. The regioselectivity of the reaction is ascertained by the nucleophilic opening of phenonium via TS-V, where attack by the pentavalent $SnBr_5^-$ anion is energetically more favorable than that by the free bromide anion by over 4 kcal/mol for TS-V-A as shown in **Figure 4.3** and **Figure 4.4**, leading to irreversible C−Br bond formation (ΔG = −16.4 or −17.3 kcal/mol). The transient nature of acyclic Int-III and the significantly higher stability of Int-IV suggest that the direct addition of bromide prior to phenonium formation is improbable.

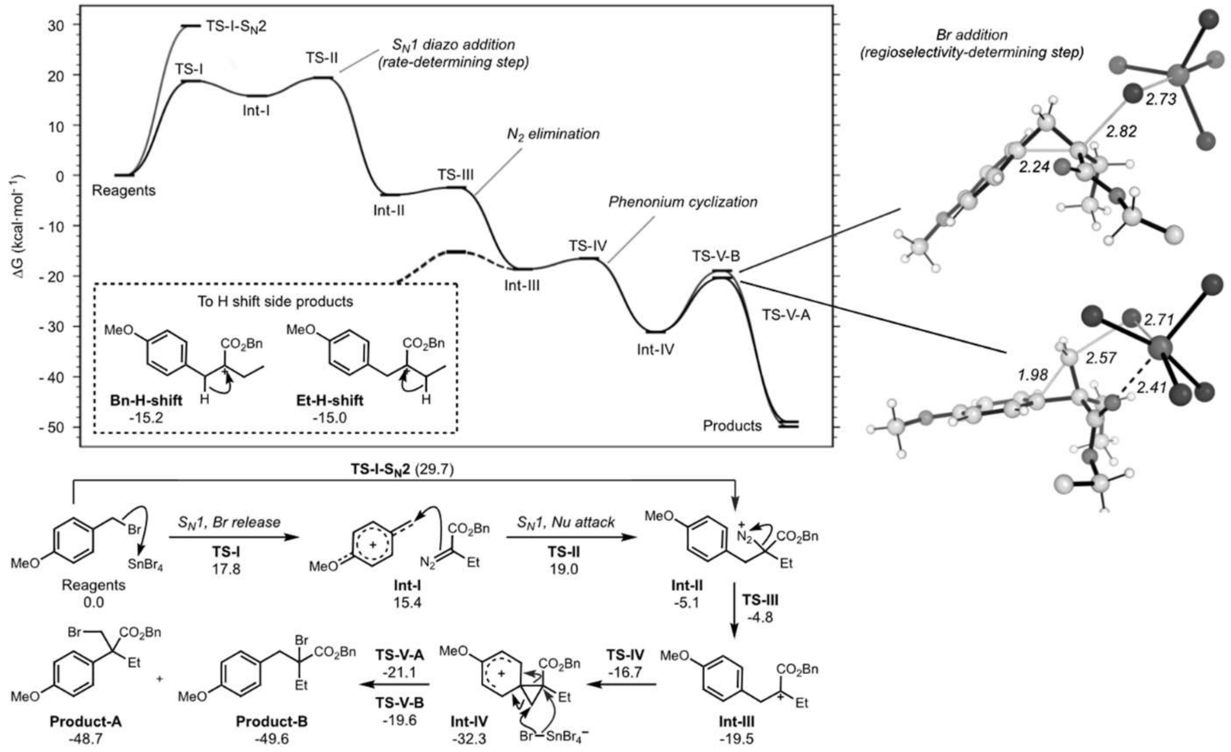

Figure 4.3 Free energy profile for model reaction.

4.3.3 Side reaction pathways

The direct capture of the tertiary carbocation (Int-III) by $SnBr_5^-$ is less energetically favorable compared to phenonium formation by a margin of 1.5 kcal/mol **(Figure 4.4)**. Despite being a less preferred route, this pathway may still offer an alternative direct avenue to product B, in conjunction to the phenonium opening through TS-V-B.

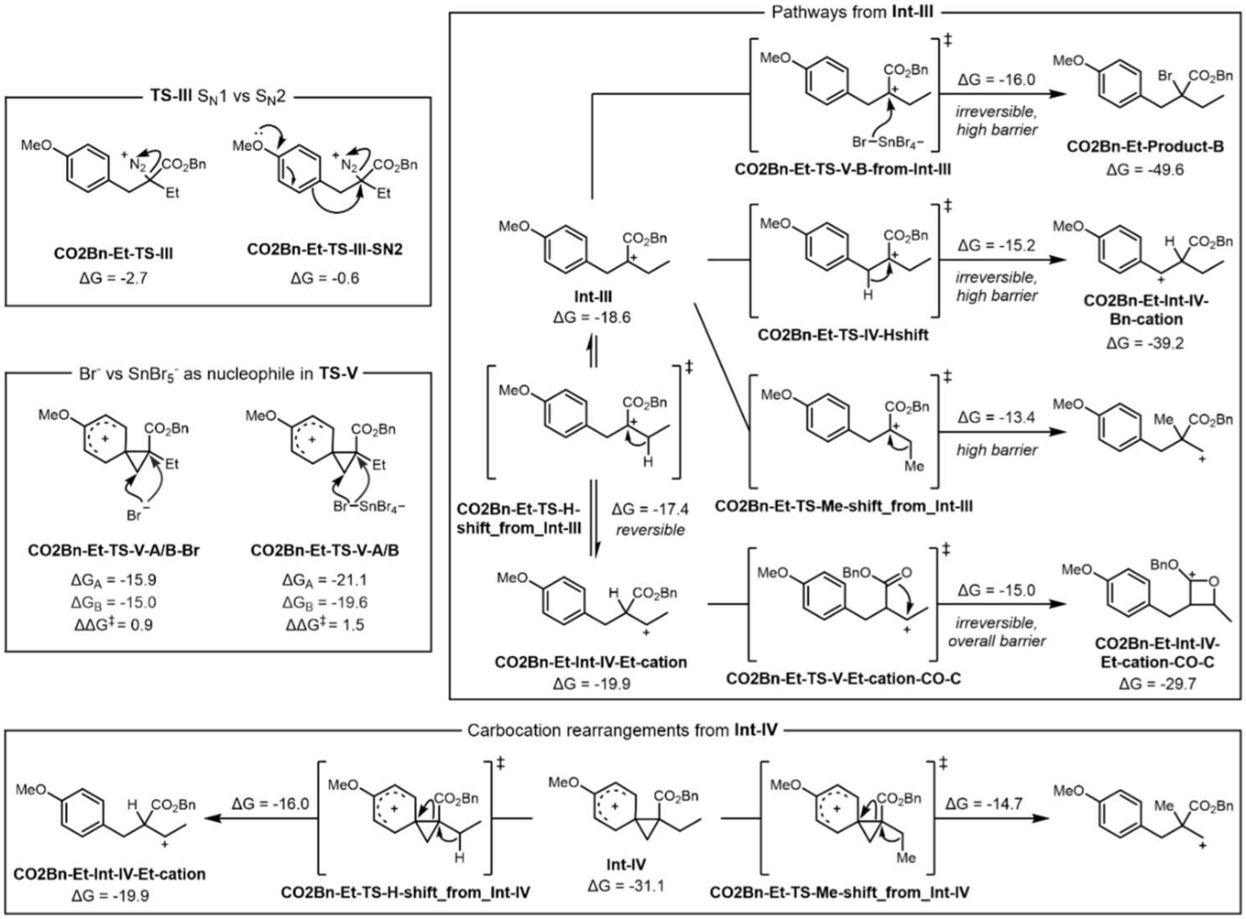

Figure 4.4 Free energies of side reaction pathways modelled without an explicit $SnBr_5^-$ counter anion.

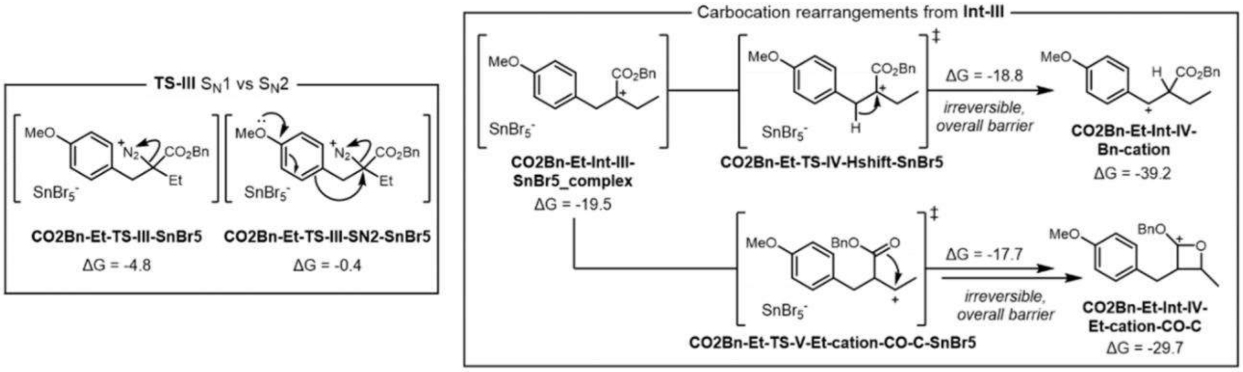

Figure 4.5 Free energies of side reaction pathways modelled with an explicit $SnBr_5^-$ counter anion.

4.3.4 Differences in regioselectivity with other substrates

We then evaluated the DFT-calculated selectivities derived from competing transition states for seven different substrate combinations against experimental outcomes. The observed trends and regioselectivities aligned well with our findings **(Figure 4.6)**. In comparison to the preferred ring-opening transition state TS-V-A, which involves a nucleophilic attack at the methylene group, the alternative, less favorable TS-V-B necessitates a larger extension of the cyclic C−C bond (by 0.26 Å) to reach the transition state, resulting in a looser and more "exploded" structure than its more stable counterpart.[19] This pattern of greater C−C bond elongation in the minor versus major transition states was consistent across all substrates examined.

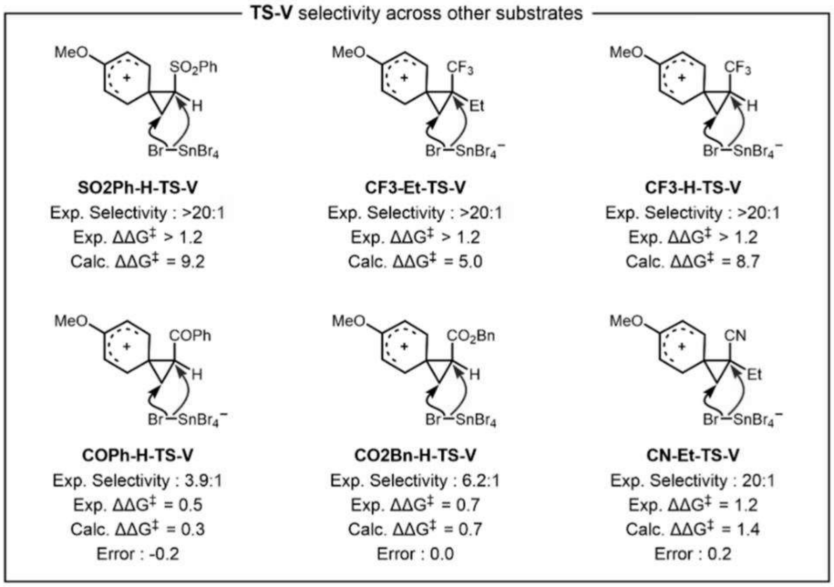

Figure 4.6 Differences in free energy between TS-V-A and TS-V-B for different substrates.

4.3.5 Quasi-Classical Molecular Dynamics simulations

We therefore initiated quasi-classical molecular dynamics trajectories[20] around the TS-II area **(Figure 4.7)**. Numerous trajectories progressed towards phenonium Int-IV, transitioning through Int-II with a notably brief average duration (262 fs, where only a handful of complete C−N vibrations were observed in several trajectories)[21] and Int-III, which exhibited a somewhat extended lifespan of 439 fs, verifying the presence of dynamic intermediates. Despite the potential energy surface being stepwise in theory, a consistent transfer of stereochemical information from the reactants to the phenonium configuration was noted in MD trajectories adhering to the primary route[22].

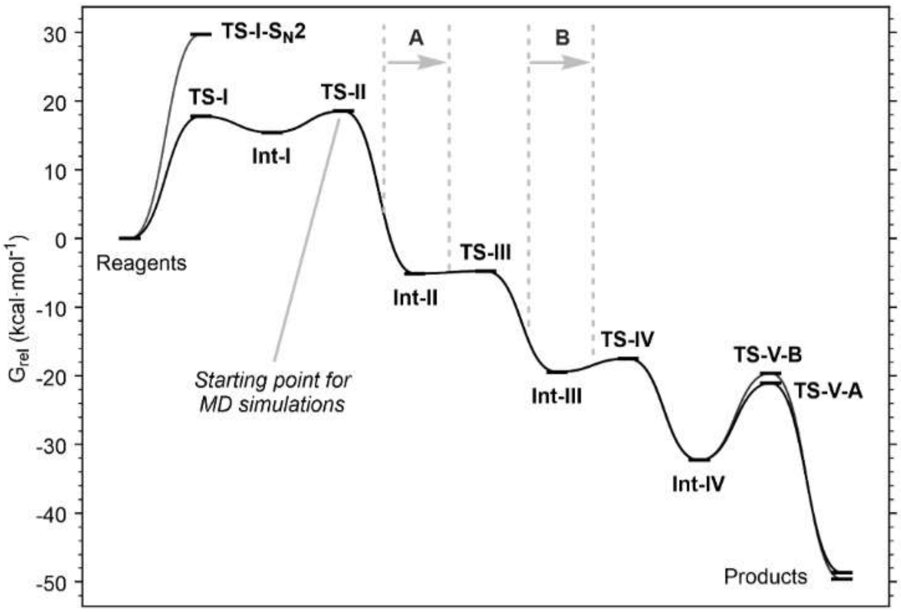

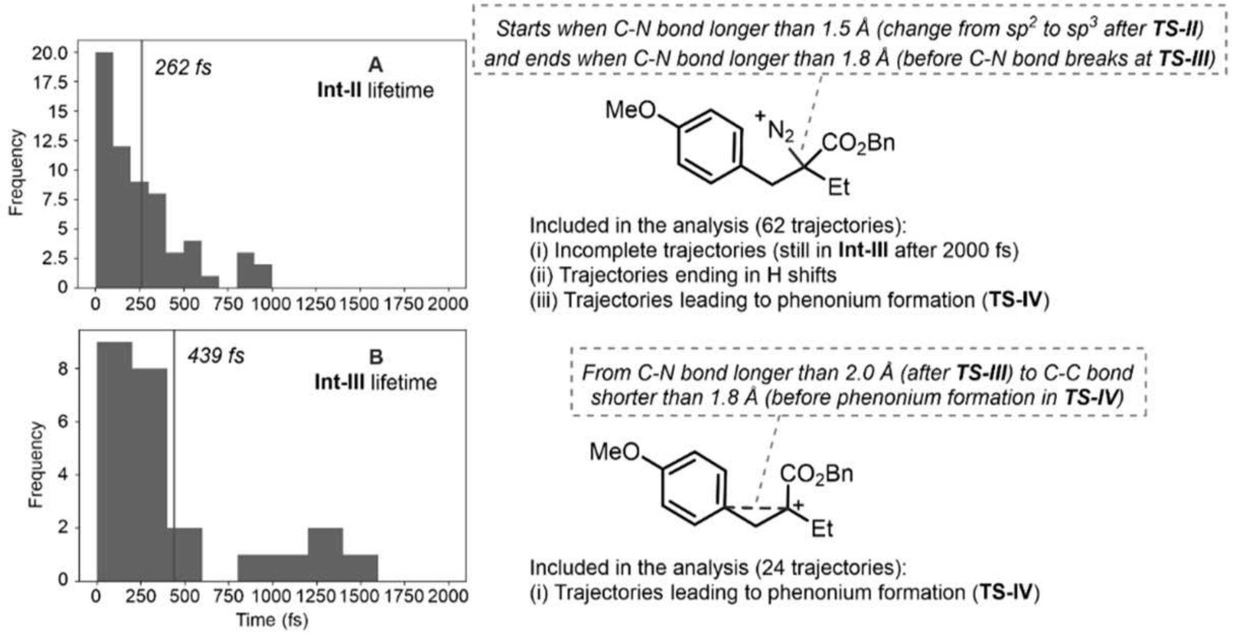

Starts when C-N bond longer than 1.5 Å (change from sp^2 to sp^3 after ***TS-II****) and ends when C-N bond longer than 1.8 Å (before C-N bond breaks at* ***TS-III****)*

Included in the analysis (62 trajectories):
(i) Incomplete trajectories (still in **Int-III** after 2000 fs)
(ii) Trajectories ending in H shifts
(iii) Trajectories leading to phenonium formation (**TS-IV**)

From C-N bond longer than 2.0 Å (after ***TS-III****) to C-C bond shorter than 1.8 Å (before phenonium formation in* ***TS-IV****)*

Included in the analysis (24 trajectories):
(i) Trajectories leading to phenonium formation (**TS-IV**)

Figure 4.7 Detailed description of lifetime calculations of Int-II and Int-III.

4.3.6 Statistical models for regioselectivity

To delve deeper into the connection between the structure of the phenonium intermediate and the experimentally observed regioselectivity, we conducted a statistical analysis. We selected structural, electronic, and chemical bonding characteristics of 24 phenonium intermediates as crucial indicators **(Figure 4.8A)**. Drawing inspiration from Sigman and Doyle's use of a single-node decision tree for mechanistic insight, our aim was to pinpoint a solitary descriptor capable of distinguishing highly regioselective from non-selective substrates.[23] Opting for a classification model over a (non)linear regression model was particularly apt given that some substrates yield a sole regioisomer (>20:1), making it impossible to precisely quantify $\Delta\Delta G^{\ddagger}$. Consequently, we categorized the experimental data based on high and low selectivity, using an experimental regioisomeric ratio (r.r.) of 13:1 ($\Delta\Delta G^{\ddagger}$ = 1 kcal/mol) as the division point. We discovered that the energy of the natural CA−CC σ* orbital was the most indicative feature, establishing an energy "threshold" (0.183 au) beneath which substrates invariably react with high regioselectivity **(Figure 4.8B)**. Phenonium ions below this energy threshold universally exhibited experimental selectivities >13:1, whereas among those above this threshold, 11 out of 14 (79%) showed low selectivity. This particular bond is irreversibly cleaved in the transition structure leading to the creation of the major regioisomer.

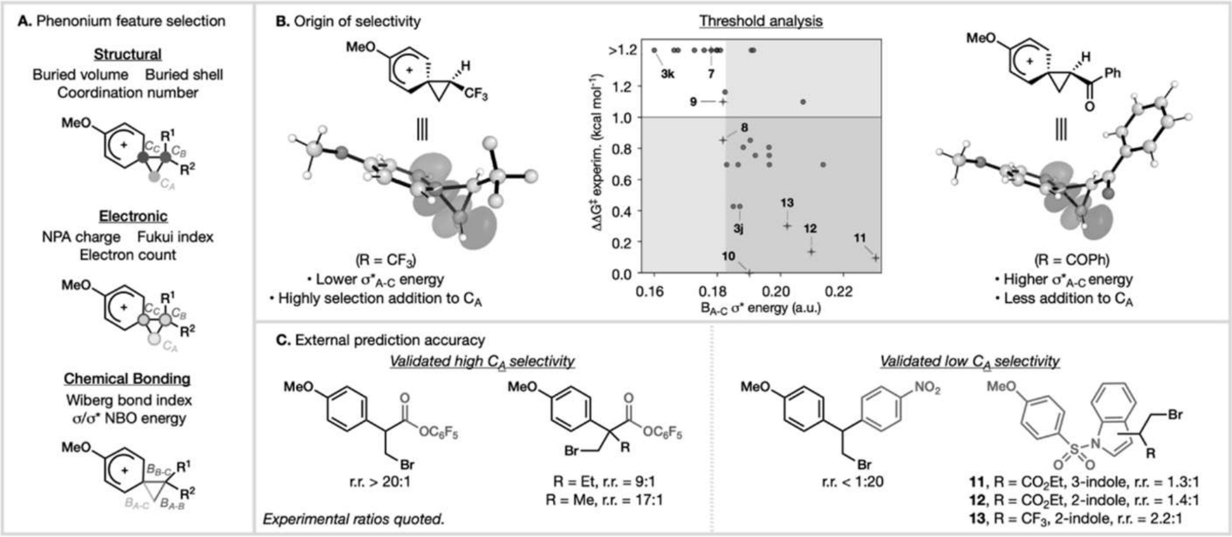

Figure 4.8 Threshold analysis for the classification of selectivity using CA-CC antibonding energy and experimental validation of the model.

To test the accuracy of this model, seven theoretically designed out-of-sample substrates with varied substituents from those in the training set were predicted for selectivity, ranging from high (7−9) to low (10−13). These classifier-generated forecasts aligned well with actual experimental findings **(Figure 4.8C)**.

4.4 Conclusions

In summary, we have developed a homologation process that pairs benzyl bromides with diazo compounds, utilizing the conventional roles of benzyl halides (as electrophiles) and aromatic rings (as nucleophiles) to facilitate the formal incorporation of a diazo group into the C(sp2)−C(sp3) bond. Through computational examination of the reaction pathway, we identified a rate-limiting S_N1 type mechanism initiating C−C bond creation, which is followed by a series of cationic intermediates culminating in the formation of a phenonium ion. This study has enhanced our understanding of the factors influencing the regioselectivity of the phenonium ion openings, allowing for the accurate a priori prediction of outcomes for novel substrate combinations. Ultimately, this research presents a versatile strategy for the synthesis of acyclic, benzylic quaternary centers, starting from common reagents, which is expected to be of significant interest in the field of drug development.

REFERENCES

1. E. J. Corey, X. M. Cheng, Wiley, (1989).

2. J. Dakka, Y. Sasson, J. Org. Chem., 54, 3224–3226 (1989).

3. U. K. Tambar, B. M. Stoltz, J. Am. Chem. Soc., 127, 5340–5341 (2005); T. Hashimoto, Y. Naganawa, K. Maruoka, J. Am. Chem. Soc., 130, 2434–2435 (2008).

4. L. Souillart, N. Cramer, Chem. Rev., 115, 9410–9464 (2015); G. Fumagalli, S. Stanton, J. F. Bower, Chem. Rev., 117, 9404–9432 (2017); Y. Xia, G. Dong, Nat. Rev. Chem., 4, 600–614 (2020).

5. F. Wang, J. Yi, Y. Nishimoto, M. Yasuda, Synthesis, 53, 4004–4019 (2021).

6. A. Ford, H. Miel, A. Ring, C. N. Slattery, A. R. Maguire, M. A. McKervey, Chem. Rev., 115, 9981–10080 (2015); N. R. Candeias, R. Paterna, P. M. P. Gois, Chem. Rev., 116, 2937–2981 (2016); N. Guttenberger, R. Breinbauer, Tetrahedron, 73, 6815–6829 (2017); S. P. Green, K. M. Wheelhouse, A. D. Payne, J. P. Hallett, P. W. Miller, J. A. Bull, Org. Process Res. Dev., 24, 67–84 (2020).

7. T. Bug, M. Hartnagel, C. Schlierf, H. Mayr, Chem. - Eur. J., 9, 4068–4076 (2003).

8. D. J. Cram, J. Am. Chem. Soc., 86, 3767–3772 (1964).

9. X. Li, C. Li, W. Zhang, X. Lu, S. Han, R. Hong, Org. Lett., 12, 1696–1699 (2010); S. Protti, D. Dondi, M. Mella, M. Fagnoni, A. Albini, Eur. J. Org. Chem., 2011, 3229–3237 (2011); J. Li, A. Bauer, G. Di Mauro, N. Maulide, Angew. Chem., Int. Ed., 58, 9816–9819 (2019); H. A. Sharma, K. M. Mennie, E. E. Kwan, E. N. Jacobsen, J. Am. Chem. Soc., 142, 16090–16096 (2020); S. Xu, H. M. Holst, S. B. McGuire, N. J. Race, J. Am. Chem. Soc., 142, 8090–8096 (2020); B. S. Martins, D. Kaiser, A. Bauer, I. Tiefenbrunner, N. Maulide, Org. Lett., 23, 2094–2098 (2021).

10. K.-T. Kang, S. T. Kim, G.-S. Hwang, D. H. Ryu, Angew. Chem., Int. Ed., 56, 3977–3981 (2017).

11. F. Lovering, J. Bikker, C. Humblet, J. Med. Chem., 52, 6752–6756 (2009); F. Lovering, MedChemComm, 4, 515–519 (2013).

12. T. Ling, F. Rivas, Tetrahedron, 72, 6729–6777 (2016); T. T. Talele, J. Med. Chem., 63, 13291–13315 (2020).

13. E. Fillion, A. Wilsily, J. Am. Chem. Soc., 128, 2774–2775 (2006); A. Bonet, M. Odachowski, D. Leonori, S. Essafi, V. K. Aggarwal, Nat. Chem., 6, 584–589 (2014); I. Marek, Y. Minko, M. Pasco, T. Mejuch, N. Gilboa, H. Chechik, J. P. Das, J. Am. Chem. Soc., 136, 2682–2694 (2014); C.-Y. Huang, A. G. Doyle, J. Am. Chem. Soc., 137, 5638–5641 (2015); P. Starkov, J. T. Moore, D. C. Duquette, B. M. Stoltz, I. Marek, J. Am. Chem. Soc., 139, 9615–9620 (2017); H. Yoon, A. D. Marchese, M. Lautens, J. Am. Chem. Soc., 140, 10950–10954 (2018); H.-H. Zhang, J.-J. Zhao, S. Yu, J. Am. Chem. Soc., 140, 16914–16919 (2018); A. E. Wendlandt, P. Vangal, E. N. Jacobsen, Nature, 556, 447–451 (2018); Y. Li, J. Han, H. Luo, Q. An, X.-P. Cao, B. Li, Org. Lett., 21, 6050–6053 (2019).

14. J. Christoffers, A. Baro, Adv. Synth. Catal., 347, 1473–1482 (2005); K. W. Quasdorf, L. E. Overman, Nature, 516, 181–191 (2014); J. Feng, M. Holmes, M. J. Krische, Chem. Rev., 117, 12564–12580 (2017); L. Süsse, B. M. Stoltz, Chem. Rev., 121, 4084–4099 (2021); W. Xue, X. Jia, X. Wang, X. Tao, Z. Yin, H. Gong, Chem. Soc. Rev., 50, 4162–4184 (2021).

15. E. P. Gillis, K. J. Eastman, M. D. Hill, D. J. Donnelly, N. A. Meanwell, J. Med. Chem., 58, 8315–8359 (2015); Y. Zhou, J. Wang, Z. Gu, S. Wang, W. Zhu, J. L. Aceña, V. A. Soloshonok, K. Izawa, H. Liu, Chem. Rev., 116, 422–518 (2016); B. M. Johnson, Y.-Z. Shu, X. Zhuo, N. A. Meanwell, J. Med. Chem., 63, 6315–6386 (2020).

16. M. Holmes, K. D. Nguyen, L. A. Schwartz, T. Luong, M. J. Krische, J. Am. Chem. Soc., 139, 8114–8117 (2017); P. K. Mykhailiuk, Chem. Rev., 120, 12718–12755 (2020).

17. Gaussian 16, Rev. C.01; Gaussian, Inc.: Wallingford, CT, 2016; NBO, ver. 7.0. E. D. Glendening, J. K. Badenhoop, A. E. Reed, J. E. Carpenter, J. A. Bohmann, C. M. Morales, P. Karafiloglou, C. R. Landis, F. Weinhold, Theoretical Chemistry Institute, University of Wisconsin, Madison, WI, 2013. Supporting Information.

18. Y. Oyola, D. A. Singleton, J. Am. Chem. Soc., 131, 3130–3131 (2009); Z. Chen, Y. Nieves-Quinones, J. R. Waas, D. A. Singleton, J. Am. Chem. Soc., 136, 13122–13125 (2014).

19. B. L. Knier, W. P. Jencks, J. Am. Chem. Soc., 102, 6789–6798 (1980).

20. E. E. Kwan, R. Y. Liu, J. Chem. Theory Comput., 11, 5083–5089 (2015).

21. K. Black, P. Liu, L. Xu, C. Doubleday, K. N. Houk, Proc. Natl. Acad. Sci. U. S. A., 109, 12860 (2012).

22. D. M. H. Ascough, F. Duarte, R. S. Paton, J. Am. Chem. Soc., 140, 16740–16748 (2018).

23. S. H. Newman-Stonebraker, S. R. Smith, J. E. Borowski, E. Peters, T. Gensch, H. C. Johnson, M. S. Sigman, A. G. Doyle, Science, 374, 301–308 (2021).

CHAPTER 5: IRIDIUM-CATALYZED ASYMMETRIC DIFUNCTIONALIZATION OF C-C SIGMA BONDS ENABLED BY RING-STRAINED BORONATE COMPLEXES.

In this chapter is presented the computational work done to elucidate the enantioselectivity and mechanism of a C-C bond formation between highly reactive nucleophile (BCB boronates) and highly reactive electrophiles (Allyl iridium).

This work is a collaboration with Hong-Cheng Shen, Ze-Shu Wang and Adam Noble from Varinder K. Aggarwal's research group and Mihai V, Popescu in Robert Paton's research group. All experimental work was performed by H.-C. Shen, Z.-S. W. and A. N. all calculations were performed by M. V. P. and L. d. L. This work was published as "Iridium-Catalyzed Asymmetric Difunctionalization of C-C σ-Bonds Enabled by Ring-Strained Boronate Complexes" in *J. Am. Chem. Soc.* (145, 30, 16508-16516, 2023).

5.1 Background and significance

Enantioenriched organoboron compounds are invaluable for the stereoselective construction of complex molecules, they are widely used across organic synthesis and drug development. The extensive utility of these compounds has spurred the creation of numerous methodologies for their synthesis,[1] such as stereospecific 1,2-metalate rearrangements of boronate complexes.[2] These processes generally involve the homologation of boronic esters with metal carbenoids, either through substrate-controlled homologation[3] or the more flexible reagent-controlled lithiation−borylation approach.[2a,d] However, catalytic enantioselective 1,2-metalate rearrangements of alkenyl boronate complexes, aiming to synthesize enantioenriched alkyl boron reagents, are comparatively less explored. Recent advancements have been made in reactions of alkenyl boronate complexes with chiral transition metal complexes, triggering a 1,2-migration from an alkyl or aryl group on boron to the adjacent sp^2 carbon.[2b,c]

Transition metal-catalyzed 1,2-metalate rearrangements of alkenyl boronates can proceed via either inner sphere (where the π-bond directly interacts with the metal) or outer sphere (where the boronate attacks a metal-bound electrophile) mechanisms.[2b,c] Morken demonstrated that these rearrangements could be achieved catalytically and enantioselectively using π-acidic late transition metal complexes, such as Pd^{II} and Ni^{II}, predominantly through an inner sphere pathway.[4,5] Other reactions with electrophilic metal complexes, like π-allyl−Pd,[6,7] π-allyl−Ir,[8] and allenylidene−copper,[9] have been reported by Ishikura, Ready, and Brown, thought to proceed via an outer sphere mechanism.

While reactions of metal complexes with C=C π-bonds to introduce two different carbon fragments are well documented, similar reactions involving C−C σ-bonds are rare due to the typical strength, inertness, and geometric inaccessibility of σ-bonds. We recently discovered that cationic Pd^{II} complexes could activate σ-bonds of bicyclo[1.1.0]butyl (BCB) boronate complexes, promoting 1,2-boronate migrations to sp^3 carbons and achieving σ-bond dicarbonation.[10] This process is driven by the high strain energy of bicyclo[1.1.0]butanes[11] and proceeds with high diastereoselectivity, producing 1,1,3-trisubstituted cyclobutanes with a cis configuration between carbon substituents. Further research suggested a concerted mechanism with antiperiplanar alignment of the migrating group and the breaking σ-bond.[12] The applications of this strategy have been extended to crafting boronic ester-substituted azetidines[13] and other cyclobutanes.[14] Despite these developments, applying this strategy to synthesize enantioenriched boron reagents has not been explored. We hypothesized that chiral π-allyl metal complexes could catalyze 1,2-metalate rearrangements of strained BCB boronate complexes, leading to diastereo- and enantioenriched cyclobutanes. We were particularly interested in π-allyl iridium complexes developed by Carreira[15,16] for their effectiveness with a wide range of nucleophiles, including alkenes.[15c] Indeed, relevant to this study, Ready demonstrated the high efficiency of Carreira's iridium-(phosphoramidite) complexes in the enantio- and diastereoselective allylation of alkenyl boronates.[8]

5.2 Experimental findings

In this work, we describe our successful efforts and the establishment of an iridium-catalyzed, asymmetric allylation-induced 1,2-metalate rearrangement of BCB boronate complexes shown in **Figure 5.1**.[17,18] This approach enables the asymmetric difunctionalization of C−C σ-bonds, yielding a range of enantioenriched 1,1,3-trisubstituted cyclobutane products with a boronic ester group amenable to further derivatization. Remarkably, the 1,2-metalate rearrangement initiated by the π-allyl-iridium complex leads to anti-addition across the C−C σ-bond. This contrasts with reactions driven by $\mathrm{Pd^{II}}$−aryl complexes and other electrophiles, which predominantly produce cis diastereoisomers through syn-addition.

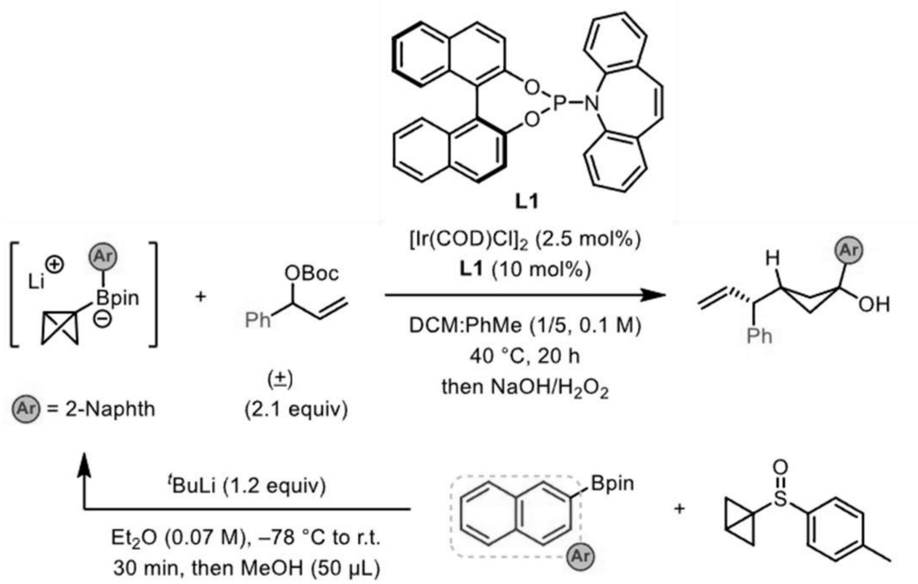

Figure 5.1 Experimental optimized conditions to achieve the desired reaction.

5.3 Computational findings

5.3.1 Methods

The hybrid density functional B3LYP,[19] in conjunction with Los Alamos LANL2DZ basis set[20] for iridium and Pople's double-zeta 6-31+G(d) basis set[21] for the remaining elements, was used to optimize all stationary point structures. Single-point energy corrections were applied to these optimized structures using the hybrid meta-GGA M06 functional[22] in conjunction with the SDD basis set[23] for iridium and Pople's triple-zeta 6-311+G(d,p) basis set for the remaining elements. For both optimization and single point calculations, the integral equation formalism variant of the polarizable continuum model (IEF-PCM), with the SMD solvation model, was applied to account for solvent effects (solvent=dichloromethane).[24] This level of theory was chosen based on a previous study by Ready and Liu[25] in the study of the allylation of vinyl boronate esters, which proved reliable when compared to experimental observations. Further benchmarking was conducted on the BCB boronate, and the results, presented in **Figure 5.2**, revealed minimal structural differences across six distinct levels of theory. Notably, the key internal C-C bond exhibited a narrow range of 1.49-1.51 Å, while all other bond lengths and dihedrals displayed very little variation across all levels of theory.

Entry	Functional	BCB-*trans* d(C–C)	BCB-*cis* d(C–C)	Overlay-*trans*
1	B3LYP	1.51	1.50	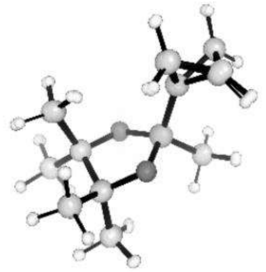
2	M06	1.49	1.49	
3	*wB97XD*	1.50	1.49	
4	TPSS	1.52	1.51	
5	PBE	1.52	1.51	
6	M06L	1.51	1.49	

Figure 5.2 Structural Benchmarking of the BCB-boronate with different functionals. All calculations were performed using the 6-31+G(d) functional in conjunction with the SMD=dichloromethane solvation model

5.3.2 Reaction of BCB-Boronate Complexes with the Tropylium Ion

Due to the considerable computational expense associated with computing the potential energy surface for the reaction between allyl-iridium complex Ir-2 and the boronates, we opted to study the full potential energy surface (PES) for a model electrophile. To this extent, we chose the reaction with the tropylium ion as a model substrate. We modeled the reaction between the tropylium ion and bicyclobutyl boronate ester (SM- tropylium) at the ωB97x-D/def2-TZVPP//ωB97x-D/6-31+G(d) level of theory in conjunction with the SMD solvation model for THF **(Figure 5.3)**. The TS leading to the formation of the cis-product was found to require an activation energy barrier of 6.0 kcal/mol, while the trans-pathway was preferred, only requiring an activation energy barrier of 5.2 kcal/mol. Compared to the reaction with an allyl-iridium electrophile, these TS geometries are later (i.e., a shorter forming C–C bond; 2.30-2.37 Å for the forming C–C bond) with larger activation energy barriers. IRC calculations performed from the cis TS were found to lead directly to the experimentally observed product in a concerted asynchronous process. There is no stable minimum on the PES corresponding to a zwitterionic intermediate, although the IRC shows a relatively flat surface after the TS (Figures S7 and S8). On the other hand, the trans-TS was found to lead to a stable local minimum corresponding to zwitterion (INT-tropylium-trans). However, 1,2-migration of the methyl group was found to proceed very rapidly with a subsequent barrier of just 0.3 kcal/mol leading to the trans-product. Therefore, we predict that C–C bond formation between the BCB and the electrophile is diastereoselectivity-determining for both products.

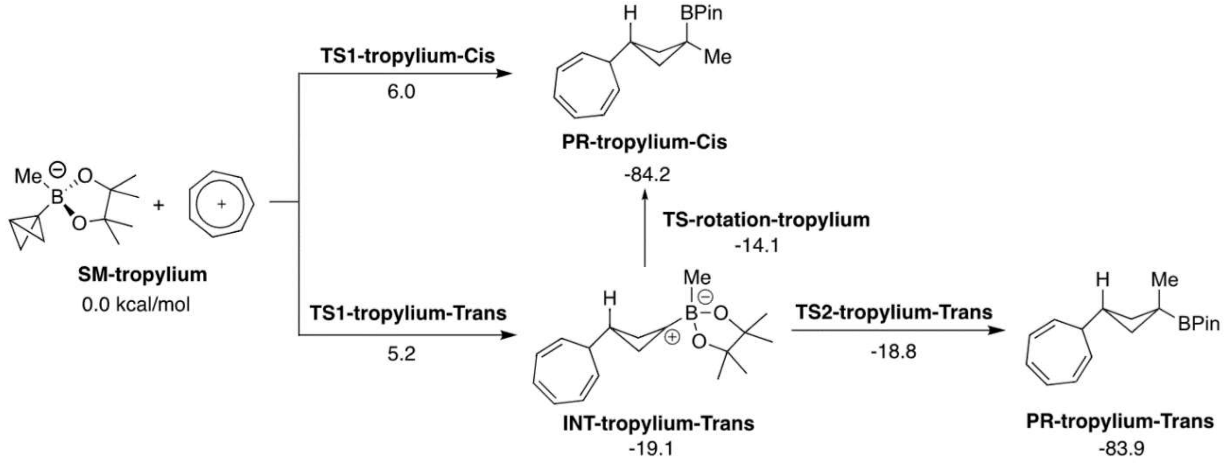

Figure 5.3 Proposed reaction mechanism for the reaction with a tropylium ion.

5.3.3 Transition structures for allylation reaction.

Therefore, to determine the origins of diastereoselectivity for the allylation reaction, we focused our attention on the C−C bond-forming TSs leading to trans- and cis-diastereomeric products for the reaction of 3b with π-allyl-iridium complex Ir-2. Note that since enantioselectivity and regioselectivity were not the focus of this study, we only computed the TSs involving the major enantiomer and major regioisomer.

The absolute sense of enantiocontrol in Ir(phosphoramidite)-catalyzed allylations with racemic allyl carbonates has been investigated computationally: oxidative addition occurs preferentially to one enantiomer (i.e., a kinetic resolution) to form a cationic π-allyl-Ir(III) complex in high enantioselectivity.[26] In this work, our computational studies focused on the origins of reactivity and diastereoselectivity in the allylation of bicyclobutyl boronates. For the reaction of the prototypical bicyclobutyl boronate substrate with a methyl group on the boron, we were able to identify 8 TS conformations for the major diastereomer of the allyl iridium complex Ir-2 that led to the trans-product and 4 TS conformations that led to the cis- product the two most stable TSs are shown in **Figure 5.4**. Equilibration of the boronate ester was studied via rotation about the C–B bond connecting the boronate group and the bicyclobutane motif. The rotational barrier was found to be 3.3 kcal/mol, similar to the activation energy barrier for the reaction with the allyl iridium complex. While rapid equilibration is challenging to assess based on the small energy differences between the two processes, it is important to consider the rate of formation of the allyl-iridium complex. Based on computational work from Ready and Liu,[27] the activation energy barrier for the formation of the allyl-iridium electrophile is estimated to be 17.6 kcal/mol (in THF). As such, due to the large energetic requirement to generate the reactive iridium catalytic species, the equilibration of rotational conformers of the substrate can be easily established as the two events (formation of allyl iridium and bond rotation) are independent of one another.

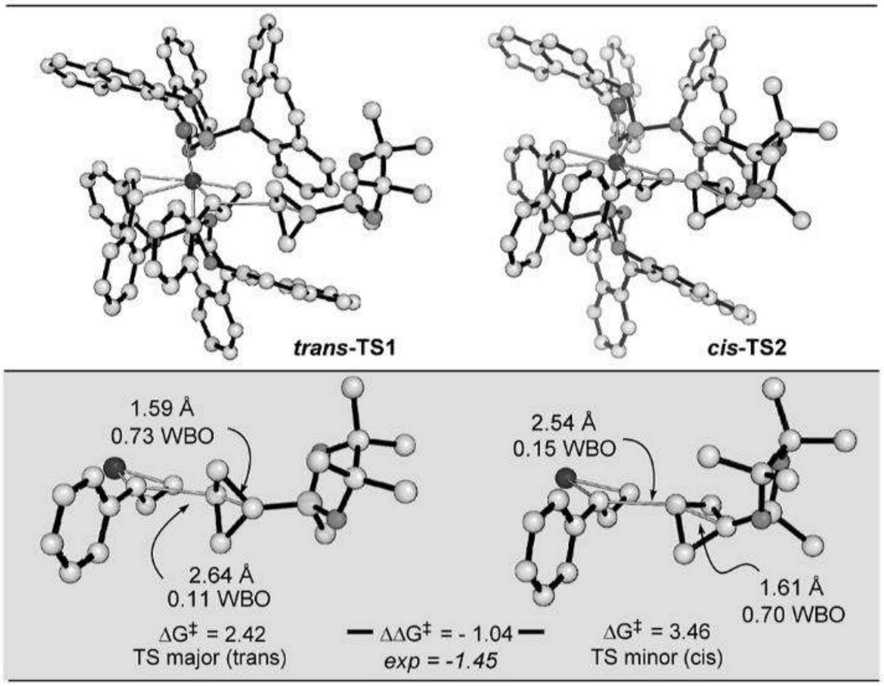

Figure 5.4 Allylation TSs. Forming C-C distances shown in Å.

5.3.4 Noncovalent interactions in allylation TSs

We calculated noncovalent interaction plot (from promolecular densities) of the most energetically favorable allylation TSs (H atoms not shown) in **Figure 5.5**. Intermolecular interactions between nucleophile and electrophile are shown, with weak dispersive interactions in green. Based on a visual comparison of the competing diastereomeric TSs, the greater stability of the trans-TS does cannot be attributed to more favorable dispersion interactions.

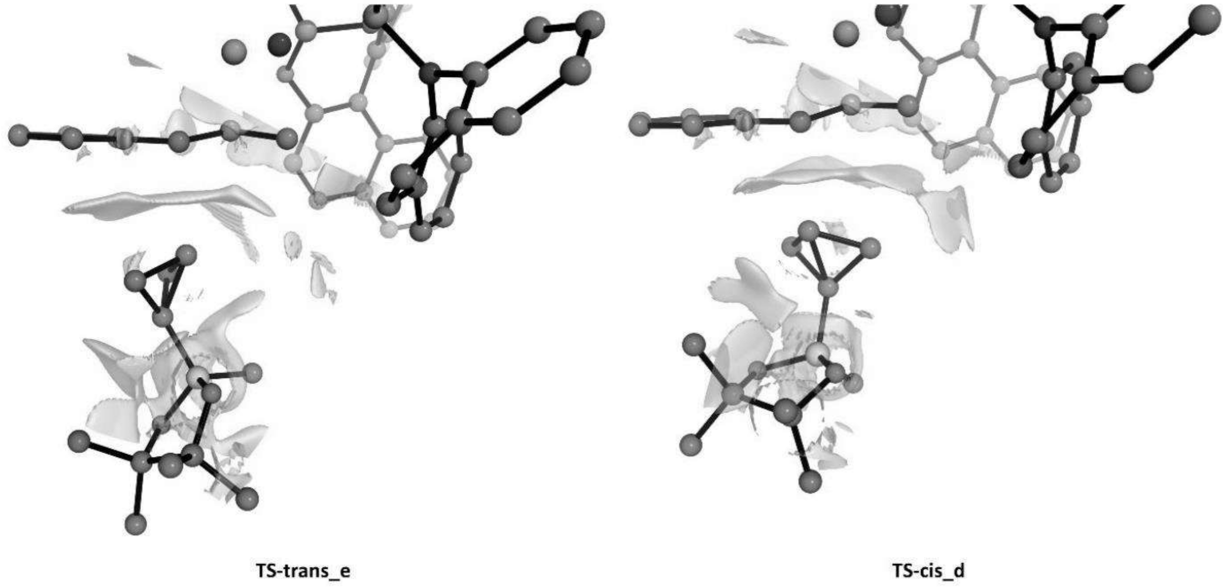

Figure 5.5 Noncovalent interaction plot for allylation TSs.

5.3.5 Rotational Barriers for BCB-Boronate Complexes and equilibrium constants

We examined this by computing rotational barriers for equilibration between the trans and cis forms of BCB boronate and related derivatives **(Figure 5.6)**, finding barriers ranging from 1.2 to 3.4 kcal/mol. For the preference between cis and trans with smaller substituents, the trans conformer is preferred to avoid steric clashes present in the cis form. For larger substituents, preferences reverse due to similar steric interactions.

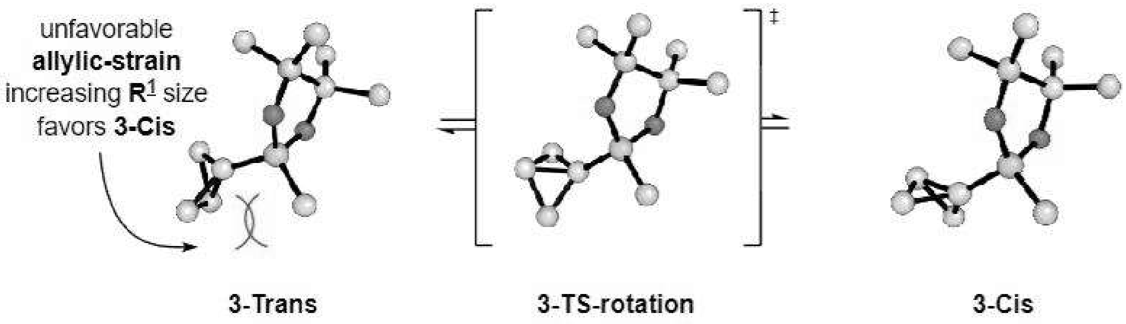

Entry	R^1	R^2	dr (*expt.*)	ΔG(DFT) / kcal·mol^{-1}	boronate structure
1	Me	H	90:10	1.18	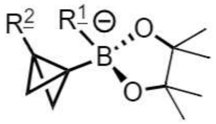
2	Ph	H	86:4	1.26	
3	*t*Bu	H	65:35	-0.77	
4	cyclohexyl	H	63:37	-0.84	
5	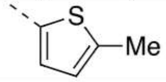	H	86:14	1.58	
6	Me	Me	94:6	2.17	
7	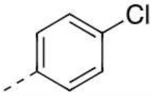	H	91:9	1.14	
8	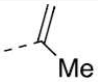	H	87:13	0.97	

Figure 5.6 Computed equilibrium conformational distribution for a series of boronate ester.

5.3.6 Rationale for enantioselectivity

The selective formation of the trans-product is particularly noteworthy, as it diverges from the cis-selective reactions of BCB boronate complexes with other electrophiles we have previously reported. We initially theorized that the preferential cis product formation was due to a stabilizing antiperiplanar orientation between the internal C−C bond of the BCB group and the B−C bond of the migrating group, present only in the transition state leading to the cis product.[28] Nonetheless, our computational analysis showed no sign of substituent migration on boron, suggesting such stabilizing effects do not play a role in the diastereoselectivity of reactions with π-allyl-iridium complexes. Another theory proposed that diastereoselectivity might be dictated by the ground-state conformation of the boronate complex. To explore this, we calculated the equilibrium conformer populations of various boronate complexes and correlated these with the experimentally observed selectivity values **(Figure 5.7)**. A strong Pearson correlation coefficient (R2 = 0.88) indicated a link between the equilibrium preferences of the boronate complexes and the experimental outcomes. Generally, the trans-conformation of the boronate complex was favored, except for cases with highly sterically hindered cyclohexyl and tert-butyl migrating groups.

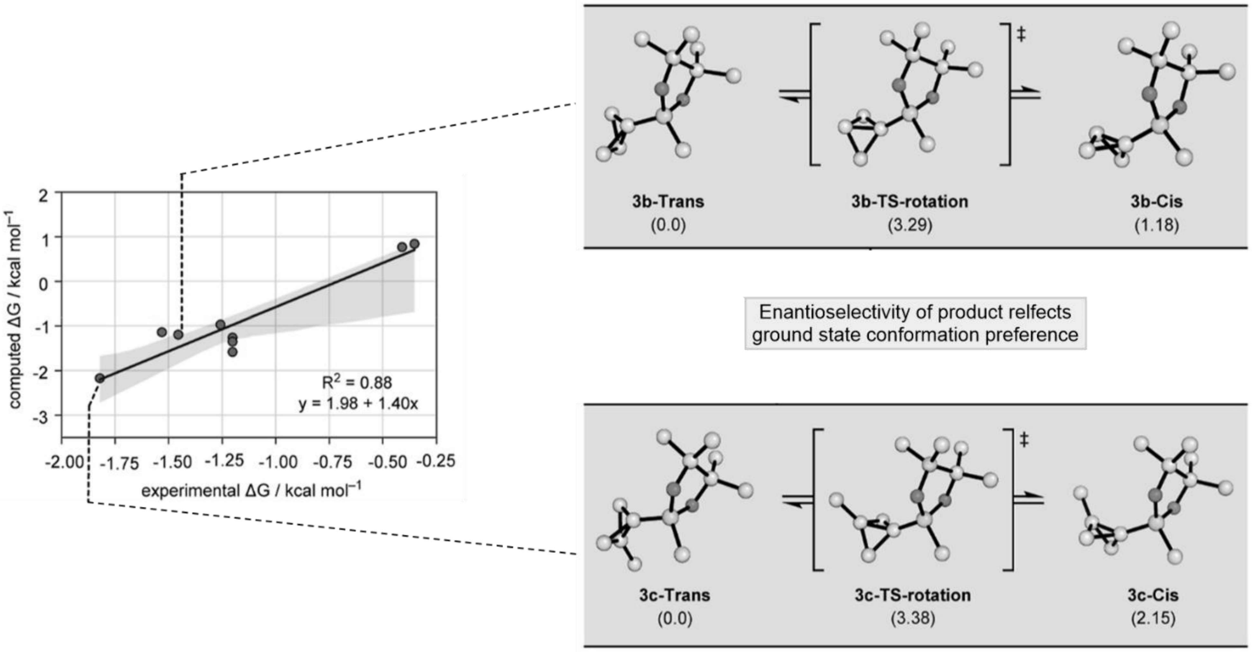

Figure 5.7 Correlation of experimentally observed selectivity with free energy difference between cis and trans configuration of the BCB boronate.

This correlation of computed ground-state energy differences with diastereoselectivity aligns with the Hammond postulate, suggesting that highly nucleophilic BCB boronates undergo early, low-barrier C−C bond-forming transition states (TSs), resembling their ground-state structure. Thus, the conformational preferences around the C−B bond are maintained in the TS, without C−B bond rotation prior to the 1,2-shift. Early TSs also reduce the significance of hyperconjugative effects, which typically favor the cis product. This explains the differing behaviors between BCB boronates with Ir and Pd complexes; with π-allyl−Ir complexes, the reaction proceeds through an early TS influenced by the ground-state conformation, leading predominantly to the trans diastereoisomer. Conversely, less reactive Pd^{II}−aryl complexes (and other electrophiles) benefit from the antiperiplanar alignment in a later TS, resulting in mainly cis diastereoisomers.

An interesting consideration is whether these reactions might bypass Curtin−Hammett control, with ground-state conformations and rates of interconversion directly affecting diastereoselectivity. Since these rotational barriers are close to those of the TS, it's challenging to definitively confirm or refute Curtin−Hammett control. However, considering previous insights from Ready et al., the energy barrier for forming the π-allyl complex is significantly higher than our computed rotational barriers, allowing enough time for thermal equilibration of the boronate complexes before each catalytic cycle of the iridium complex, suggesting Curtin−Hammett control is probable for this reaction.

5.4 Conclusions

In summary, we have described an Ir-catalyzed asymmetric allylation-induced 1,2-boronate migration, leading to the difunctionalization of C−C σ-bonds of strained boronate complexes. The methodology enables the modular synthesis of 1,1,3-trisubstituted cyclobutyl boronic esters with very high enantioselectivity and moderate to excellent diastereoselectivity. The versatile reactivity of organoboron compounds makes these products valuable building blocks for accessing enantioenriched three-dimensional cyclobutanes, which are present in a broad range of natural products and drugs. More importantly, this process unveils a new strategy for asymmetric difunctionalization of C−C σ-bonds, including dicarbonation and carboboration. Computational studies of competing allylation TSs are consistent with the experimentally observed selectivity for the trans-diastereoisomer. The BCB boronate complexes are highly nucleophilic and react via early transition states with low activation barriers, with the diastereoselectivity reflecting the ground-state conformational preference of the BCB boronate substrates, in accordance with Hammond's postulate.

REFERENCES

1. (a) S. G. Aiken, J. M. Bateman, V. K. Aggarwal, Thieme: Stuttgart, 2019; pp 393–458. (b) B. S. L. Collins, C. M. Wilson, E. L. Myers, V. K. Aggarwal, *Angew. Chem. Int. Ed.*, 56, 11700–11733 (2017). (c) D. G. Hall, in Boronic Acids, 2nd ed.; D. G. Hall, Ed.; Wiley VCH: Weinheim, 2011; pp 1–135.

2. (a) D. Leonori, V. K. Aggarwal, *Acc. Chem. Res.*, 47, 3174–3183 (2014). (b) S. Namirembe, J. P. Morken, *Chem. Soc. Rev.*, 48, 3464–3474 (2019). (c) H. Wang, C. Jing, A. Noble, V. K. Aggarwal, *Angew. Chem. Int. Ed.*, 59, 16859–16872 (2020). (d) K. Yeung, R. C. Mykura, V. K. Aggarwal, *Nat. Synth.*, 1, 117–126 (2022).

3. (a) D. S. Matteson, R. Ray, *J. Am. Chem. Soc.*, 102, 7590–7591 (1980). (b) D. S. Matteson, K. M. Sadhu, *J. Am. Chem. Soc.*, 105, 2077–2078 (1983). (c) D. S. Matteson, Acc. Chem. Res., 21, 294–300 (1988). (d) D. S. Matteson, *J. Org. Chem.*, 78, 10009–10023 (2013). (e) D. S. Matteson, B. S. L. Collins, V. K. Aggarwal, E. Ciganek, P. A. Evans, *Org. React.*, 105, 427–860 (2021).

4. (a) L. Zhang, G. J. Lovinger, E. K. Edelstein, A. A. Szymaniak, M. P. Chierchia, J. P. Morken, *Science*, 351, 70–74 (2016). (b) G. J. Lovinger, M. D. Aparece, J. P. Morken, *J. Am. Chem. Soc.*, 139, 3153–3160 (2017). (c) E. K. Edelstein, S. Namirembe, J. P. Morken, *J. Am. Chem. Soc.*, 139, 5027–5030 (2017). (d) J. A. Myhill, L. Zhang, G. J. Lovinger, J. P. Morken, *Angew. Chem. Int. Ed.*, 57, 12799–12803 (2018). (e) J. A. Myhill, C. A. Wilhelmsen, L. Zhang, J. P. Morken, J. Am. Chem. Soc., 140, 15181–15185 (2018). (f) M. D. Aparece, W. Hu, J. P. Morken, *ACS Catal.*, 9, 11381–11385 (2019). (g) Y. Meng, Z. Kong, J. P. Morken, *Angew. Chem. Int. Ed.*, 59, 8456–8459 (2020). (h) C. Law, E. Kativhu, J. Wang, J. P. Morken, *Angew. Chem. Int. Ed.*, 59, 10311–10315 (2020). (i) C. A. Wilhelmsen, X. Zhang, J. A. Myhill, J. P. Morken, *Angew. Chem. Int. Ed.*, 61, No. e202116784 (2022).

5. (a) M. Chierchia, C. Law, J. P. Morken, *Angew. Chem. Int. Ed.*, 56, 11870–11874 (2017). (b) G. J. Lovinger, J. P. Morken, *J. Am. Chem. Soc.*, 139, 17293–17296 (2017). (c) C. Law, Y. Meng, S. M. Koo, J. P. Morken, *Angew. Chem., Int. Ed.*, 58, 6654–6658 (2019). (d) M. P. Chierchia, P. Xu, G. J. Lovinger, J. P. Morken, *Angew. Chem., Int. Ed.*, 58, 14245–14249 (2019). (e) S. M. Koo, A. J. Vendola, S. N. Momm, J. P. Morken, *Org. Lett.*, 22, 666–669 (2020).

6. (a) M. Ishikura, M. Terashima, *J. Chem. Soc. Chem. Commun.*, 1991, 1219–1221. (b) M. Ishikura, H. Kato, *Tetrahedron*, 58, 9827–9838 (2002). (c) M. Ishikura, W. Ida, K. Yanada, *Tetrahedron*, 62, 1015–1024 (2006).

7. (a) S. Panda, J. M. Ready, *J. Am. Chem. Soc.*, 139, 6038–6041 (2017). (b) S. Panda, J. M. Ready, *J. Am. Chem. Soc.*, 140, 13242–13252 (2018).

8. (a) C. R. Davis, I. K. Luvaga, J. M. Ready, *J. Am. Chem. Soc.*, 143, 4921–4927 (2021). (b) C. R. Davis, Y. Fu, P. Liu, J. M. Ready, *J. Am. Chem. Soc.*, 144, 16118–16130 (2022).

9. A. K. Simlandy, M. K. Brown, *Angew. Chem., Int. Ed.*, 60, 12366–12370 (2021).

10. A. Fawcett, T. Biberger, V. K. Aggarwal, *Nat. Chem.*, 11, 117–122 (2019).

11. For selected reviews on transformations enabled by strain release, see: (a) K. B. Wiberg, *Angew. Chem., Int. Ed. Engl.*, 25, 312–322 (1986). (b) P. R. Khoury, J. D. Goddard, W. Tam, Tetrahedron, 60, 8103–8112 (2004). (c) J. Turkowska, J. Durka, D. Gryko, *Chem. Commun.*, 56, 5718–5734 (2020). (d) M. Andresini, L. Degennaro, R. Luisi, *Org. Biomol. Chem.*, 18, 5798–5810 (2020).

12. S. H. Bennett, A. Fawcett, E. Denton, T. Biberger, V. Fasano, N. Winter, V. K. Aggarwal, *J. Am. Chem. Soc.*, 142, 16766–16775 (2020).

13. A. Fawcett, A. Murtaza, C. H. U. Gregson, V. K. Aggarwal, *J. Am. Chem. Soc.*, 141, 4573–4578 (2019).

14. (a) M. Silvi, V. K. Aggarwal, *J. Am. Chem. Soc.*, 141, 9511–9515 (2019). (b) L. Guo, A. Noble, V. K. Aggarwal, *Angew. Chem., Int. Ed.*, 60, 212–216 (2021). (c) L. Lewis-Borrell, M. Sneha, I. P. Clark, V. Fasano, A. Noble, V. K. Aggarwal, A. J. Orr-Ewing, *J. Am. Chem. Soc.*, 143, 17191–17199 (2021).

15. For selected examples, see: (a) M. Lafrance, M. Roggen, E. M. Carreira, *Angew. Chem. Int. Ed.*, 51, 3470–3473 (2012). (b) J. Y. Hamilton, D. Sarlah, E. M. Carreira, *J. Am. Chem. Soc.*, 135, 994–997 (2013). (c) J. Y. Hamilton, D. Sarlah, E. M. Carreira, *J. Am. Chem. Soc.*, 136, 3006–3009 (2014). (d) S. Krautwald, M. A. Schafroth, D. Sarlah, E. M. Carreira, *J. Am. Chem. Soc.*, 136, 3020–3023 (2014). (e) J. Y. Hamilton, N. Hauser, D. Sarlah, E. M. Carreira, *Angew. Chem., Int. Ed.*, 53, 10759–10762 (2014). (f) D. A. Petrone, M. Isomura, I. Franzoni, S. L. Rössler, E. M. Carreira, *J. Am. Chem. Soc.*, 140, 4697–4704 (2018). (g) T. Sandmeier, F. W. Goetzke, S. Krautwald, E. M. Carreira, *J. Am. Chem. Soc.*, 141, 12212–12218 (2019).

16. S. L. Rössler, S. Krautwald, E. M. Carreira, *J. Am. Chem. Soc.*, 139, 3603–3606 (2017).

17. (a) R. Takeuchi, M. Kashio, *Angew. Chem., Int. Ed.*, 36, 263–265 (1997). (b) J. P. Janssen, G. Helmchen, Tetrahedron Lett., 38, 8025–8026 (1997). (c) R. Takeuchi, M. Kashio, *J. Am. Chem. Soc.*, 120, 8647–8655 (1998).

18. For selected reviews, see: (a) J. F. Hartwig, L. M. Stanley, *Acc. Chem. Res.*, 43, 1461–1475 (2010). (b) S. L. Rössler, D. A. Petrone, E. M. Carreira, *Acc. Chem. Res.*, 52, 2657–2672 (2019). (c) Q. Cheng, H.-F. Tu, C. Zheng, J.-P. Qu, G. Helmchen, S.-L. You, *Chem. Rev.*, 119, 1855–1969 (2019). (d) T. Sawano, R. Takeuchi, *Catal. Sci. Technol.*, 12, 4100–4112 (2022).

19. For an overview of stereospecific organoboronate transformations, see: C. Sandford, V. K. Aggarwal, *Chem. Commun.*, 53, 5481–5494 (2017).

20 .(a) A. Bonet, M. Odachowski, D. Leonori, S. Essafi, V. K. Aggarwal, *Nat. Chem.*, 6, 584–589 (2014). (b) R. J. Armstrong, W. Niwetmarin, V. K. Aggarwal, *Org. Lett.*, 19, 2762–2765 (2017).

21. E. Vedejs, M. Jure, *Angew. Chem., Int. Ed.*, 44, 3974–4001 (2005).

22. (a) K. Feeney, G. Berionni, H. Mayr, V. K. Aggarwal, *Org. Lett.*, 17, 2614–2617 (2015). (b) C. García-Ruiz, J. L. Y. Chen, C. Sandford, K. Feeney, P. Lorenzo, G. Berionni, H. Mayr, V. K. Aggarwal, *J. Am. Chem. Soc.*, 139, 15324–15327 (2017).

23. C. Defieber, M. A. Ariger, P. Moriel, E. M. Carreira, *Angew. Chem., Int. Ed.*, 46, 3139–3143 (2007).

24. (a) J. A. Raskatov, M. Jakel, B. F. Straub, F. Rominger, G. Helmchen, *Chem. Eur. J.*, 18, 14314–143 (2012).

25. Quantum chemical calculations were performed with Frisch, M. J.; et al. Gaussian 16, Revision C.01; Gaussian, Inc.: Wallingford CT, (2016).

26. T. Perger, A. I. Sanhueza, I. Kalvet, F. Schoenebeck, *Chem. Rev.* , 115, 9532−9586 (2015).